Thesis for the Degree of Licentiate of Engineering

Improved PEGylation of Gold Nanoparticles for Quantitative Off-Axis Holography-based Detection of Biological Nanoparticles

JULIA ANDERSSON

CHALMERS
UNIVERSITY OF TECHNOLOGY

Department of Physics
Division of Nano and Biophysics
Chalmers University of Technology
Gothenburg, Sweden 2025

Improved PEGylation of Gold Nanoparticles for Quantitative Off-Axis Holography-based Detection of Biological Nanoparticles

JULIA ANDERSSON

Department of Physics
Chalmers University of Technology
SE-412 96 Gothenburg
Telephone +46 31 772 1000

Cover: Illustrative representation of streptavidin in suspension binding to a biotin-modified PEGylated gold nanoparticle, functionalized with PEG at varying chain lengths.

Printed by Chalmers Digitaltryck
Gothenburg, Sweden 2025

Improved PEGylation of Gold Nanoparticles for Quantitative Off-Axis Holography-based Detection of Biological Nanoparticles

JULIA ANDERSSON
Department of Physics
Chalmers University of Technology
Gothenburg, Sweden 2025

Abstract

A central aspect of modern diagnostics is the detection of biomarkers, which calls for both sensitive and specific biosensing technologies. Biosensors are devices which based on various physicochemical principles are able to detect biomarkers by incorporating target-specific biological components. Due to their unique optical properties, gold nanoparticles (AuNPs) are often a core component of such techniques. The aim of this thesis is to investigate the use of twilight off-axis holographic microscopy combined with surface-modified AuNPs to specifically detect optically faint biological nanoparticles. In Paper I, twilight off-axis holography is introduced and the ability to verify detection based on material properties is investigated. It is demonstrated that by analyzing the real and imaginary parts of the complex-valued optical field, metallic particles can be discerned from dielectric material. Moreover, it is shown that dielectric particles below the detection limit can, through complex formation with functionalized AuNPs, be detected and quantified based on refractive index. In Paper II, this approach was further developed for the use of twilight off-axis holography for specific detection of biotin-modified lipid vesicles. To form specific complexes between AuNPs and biotinylated lipid vesicles, AuNPs were surface modified with streptavidin via biotinylated PEG attached to the AuNPs. Using holographic microscopy, waveguide scattering microscopy and surface plasmon resonance, it was demonstrated that surrounding non-biotinylated PEG may sterically hinder streptavidin-biotin interaction, requiring a thousandfold excess of streptavidin. By decreasing the molecular weight of non-biotinylated PEG, the biotin accessibility was significantly increased and streptavidin-modified AuNPs could be fabricated without the need for excessive protein consumption. Through complex formation with these AuNPs, lipid vesicles could be detected using twilight off-axis holographic microscopy with a sub-pM level of detection.

Keywords: Gold nanoparticles, Polyethylene glycol, Lipid vesicles, Surface modification, Holographic microscopy, Waveguide scattering microscopy, Surface plasmon resonance, Bioanalytical sensing

List of Publications

This thesis is based on the following publications:

Paper I:

Label-Free Optical Quantification of Material Composition of Suspended Virus-Gold Nanoparticle Complexes
Erik Olsén, Julia Andersson, Benjamin Midtvedt, Adrián González, Fredrik Eklund, Katarzyna Ranoszek-Soliwoda, Jaroslaw Grobelny, Giovanni Volpe, Malgorzata Krzyzowska, Fredrik Höök, and Daniel Midtvedt
In manuscript

Contribution: JA fabricated some of the material, performed part of the holographic measurements and contributed to the writing of the paper.

Paper II:

Quantitative Detection of Biological Nanoparticles Using Twilight Off-Axis Holographic Microscopy: Insights on Complex Formation between PEGylated Gold Nanoparticles and Lipid Vesicles
Julia Andersson, Anders Lundgren, Erik Olsén, Petteri Parkkila, Daniel Midtvedt, Björn Agnarsson, and Fredrik Höök
In manuscript

Contribution: JA was responsible for designing and performing all experiments as well as manuscript preparation.

Publications not included in the thesis:

The Inhibition of Fibril Formation of Lysozyme by Sucrose and Trehalose
Kajsa Ahlgren, Fritjof Havemeister, Julia Andersson, Elin K. Esbjörner, and Jan Swenson
RSC Adv., 2024,14, 11921-11931

Acknowledgements

Firstly, I want to thank Fredrik Höök, my supervisor, for giving me this opportunity, for his guidance and for being a constant inspiration. I would also like to thank Daniel and Hana, my co-supervisors, for their support and advice. I can always count on you to have helpful insights and ideas.

My gratitude extends to Mikael Käll, my examiner. Thank you for always making sure we don't stray too far from physics.

A massive thank you to Anders and Björn for your tireless and endlessly enthusiastic help and support. And thank you to Erik for all your guidance and for helping me find my footing as a new student.

To Kajsa, a big thank you for filling the office with cheer and laughter. Thank you to Emelie for keeping the office couch warm and reminding me that TikTok is for children. To Simon, Björn, Petteri, Nima, Mattias, Nastaran, Achilleas, Julie, Jan, and all former members of the biophysics group, thank you for all the entertaining and interesting fika sessions. And a special thank you to Kajsa, Björn, Petteri and Erik for helping me proofread the thesis.

Thank you to the girls, for much needed lunch breaks and for all the laughs and rants.

Lovisa, even back all those years ago, during our late nights editing that stupid cabaret video, I knew I had found a lifelong friend. Having you in my life is one of my greatest honors. You're the best thing to ever come out of Torslanda.

To Linus, who has been by my side since our very first day at Chalmers, almost 8 years ago. Your endless kindness, generosity and humor have kept me afloat through all these years. Chalmers wouldn't be the same without you.

To my parents and my brother, thank you for always being the solid ground beneath my feet. Every single step I have taken, you have been right there beside me. I will be forever grateful for your endless support and love. And to the rest of my friends and family, thank you for always encouraging me, for all your joy and warmth.

Julia Andersson, Gothenburg, 2025

List of Acronyms

Below is an alphabetically ordered list of the acronyms used in this thesis:

AuNP	Gold Nanoparticle
Biotin-LUV	Biotinylated large unilamellar lipid vesicle
BSA	Bovine serum albumin
CAR	Chimeric Antigen Receptor
DBCO	Dibenzocyclooctyne
DLS	Dynamic light scattering
DSPE	1,2-distearoyl-sn-glycero-3-phosphoethanolamine
LFAF	Low-frequency attenuation filter
LNP	Lipid nanoparticle
NTA	Nanoparticle tracking analysis
PBS	Phosphate-buffered saline
PEG	Polyethylene glycol
SH-PEG	Thiol-terminated PEG
POPC	1-palmitoyl-2-oleoyl-sn-glycero-3-phosphocholine
RI	Refractive index
SAM	Self-assembled monolayer
SPR	Surface plasmon resonance
StrAv	Streptavidin
StrAv-AuNP	AuNP modified with StrAv via PEG linkers
TEM	Transmission electron microscopy
TIR	Total internal reflection
tLNP	Targeting LNP
UV-Vis	Ultraviolet-visible spectroscopy
WGSM	Waveguide scattering microscopy

Contents

List of Figures

1

Introduction

Medical diagnostics have been performed since antiquity, at which time diagnoses were bound by sensory observations [1]. This mainly involved sight and hearing [2], but physicians in various cultures would both smell and taste bodily fluids [3]. These methods were, of course, often insufficient for proper diagnosis, which combined with lacking knowledge of human anatomy and physiology severely hampered positive medical outcomes [4]. Throughout history, our medical knowledge has increased enormously. Detailed knowledge of anatomical function and revolutionary tools for both diagnostics and treatment have significantly advanced modern medicine and improved patient care. While we, in a way, still rely on our senses, we now utilize diverse physicochemical principles and advanced instruments such as magnetic resonance imaging scanners and X-ray machines to heighten them far beyond human capacity.

A crucial aspect of modern medical diagnostics is the detection of specific biomarkers. Whether it concerns the detection of viral antigens to identify infection, tumor-secreted molecules to diagnose certain cancers, or protein biomarkers to monitor diabetes, the development of accurate methods for detecting specific biological molecules is essential [5]. This can be achieved using a biosensor, which is an analytical device designed for the detection of specific chemical compounds based on the combination of biological components with a physicochemical detector [6]. Such devices require two constituents. The first is some biological or biomimetic component which specifically binds to or otherwise interacts with the biomarker. The other part is a transducer, which converts this interaction into a detectable signal. By utilizing physicochemical phenomena such as piezoelectricity, electrochemistry or light-matter interaction, biomolecular interactions can be observed and analyzed.

Since small variations in the concentration of biomarkers typically occur with disease progression [7, 8], early diagnosis requires sensitive biosensors. Moreover, to avoid misdiagnosis, highly specific sensors are essential. In addition to these fundamental requirements, aspects such as ease of use and sample volume ought to be considered as well. Biosensors can be designed using a wide range of approaches, which has led to the development of various types of sensors. For instance, optical biosensors probe the interaction of light and matter through e.g. absorption, scattering and fluorescence to enable direct, often label-free detection of biological substances [9], while piezoelectric biosensors detect changes in mass through shifts in resonance frequency [10]. These are both examples of different approaches to designing the transducer, which can then be combined with biological components

specifically matched to the diagnostic target to produce a biosensor.

A common foundation of many biosensors is gold, due to its various unique physical and optical properties [11], many of which are highly useful for the design of biosensor transducers. Gold is also stable, biocompatible and highly versatile, which facilitates integration of the biological component. Owing to the versatility of gold, both with respect to morphology and surface modification, there are many approaches to incorporate gold in biosensing. For instance, thin gold films can be utilized in surface-based sensors such as quartz crystal microbalance [10], surface plasmon resonance [12] and surface-enhanced Raman spectroscopy [13]. Gold is frequently used in biosensing in the form of nanostructures, especially gold nanoparticles (AuNPs). The integration of AuNPs in various established biosensors has been shown to increase their sensitivity immensely [14]. For instance, detection of DNA hybridization using gold-enhanced SPR demonstrated a thousandfold increase in sensitivity over unamplified detections, as a result of the material and optical properties of AuNPs [15].

In addition to enhancing established techniques, novel AuNP-based biosensors have been demonstrated as well. Typical categories include electrochemical, pizeoelectric and optical methods [14, 16]. Electrochemical biosensors are based on changes in electrical characteristics, and AuNPs are typically applied as a platform for immobilization or a reaction catalyst [14, 17, 18]. Piezoelectricity is a property of certain materials for which an electric current can induce mechanical stress, and vice versa [10]. When excited by an electric current, a piezoelectric material will vibrate at a specific resonant frequency. Since this frequency is dependent on mass, piezoelectric biosensors can temporally probe changes in mass on the surface. In such assays, the high density of AuNPs has been utilized to amplify the mass change [16]. Optical biosensing methods typically refer to techniques which measure how light waves are altered by an analyte. Due to the various unique optical properties of AuNPs (see Section 2.1.1), such methods encompass a variety of approaches [19]. A particularly exploited attribute of AuNPs is their plasmonic property [9, 20]. Many such biosensors are colorimetric, which means they are based on the interparticle distance dependence [21–23] of the plasmonic coupling of AuNPs, which causes detectable, and often visible, changes in color [24]. By conjugating AuNPs with analyte-specific ligands, the presence of analytes can induce AuNP aggregation. If the AuNPs accumulate in sufficiently close proximity, a colorimetric shift will occur, through which specific analytes may be detected.

While numerous colorimetric biosensors have been developed, an inherent limitation of such methods is the range of the plasmonic effects. Specifically, when the interparticle separation exceeds approximately the particle diameter [25, 26], plasmonic coupling no longer occurs. AuNPs often require surface modification for e.g. passivation and bioconjugation. The size of these surface modification agents often exceeds the limitations of plasmonic coupling, which prevents colorimetric shifts from occurring upon aggregation. In such cases, non-colorimetric aggregation-based methods are needed. In the following thesis, a new use of holographic microscopy

as a biosensor is presented, wherein twilight off-axis holography is utilized to detect biological nanoparticles based on the possibility of making a distinction between metallic and dielectric material. In paper I, twilight off-axis holographic microscopy is introduced and simultaneous estimation of hydrodynamic size and the ability to detect bioloigcal nanoparticles below the detection limit through quantitative differentiation between signals from metal and dielectric nanoparticles is demonstrated. In paper II, this method is further developed for detection of optically faint biological nanoparticles through induced aggregation with functionalized AuNPs. Specifically, the PEGylation of AuNPs to facilitate subsequent streptavidin modification, enabling complex formation with biotinylated lipid vesicles, is investigated and developed.

The thesis will first present background theory on key concepts and experimental methods. Theoretical background on relevant material and physical principles is outlined in Chapter 2, followed by foundational theory on experimental techniques and fabrication methods in Chapter 3 and more detailed experimental procedures in Chapter 4. Finally, the results of Paper I and Paper II are summarized in Chapter 5, while Chapter 6 presents the outlook for future research.

2

Theoretical Background

2.1 Gold Nanoparticles

Any discussion of the history and properties of AuNPs would be sorely lacking without a nice picture of a colorful church window or an old roman cup (both of which can of course be seen in Fig. 2.1). These two, the famous Lycurgus cup from the 4th century and our long history of glass staining, are classic examples of how the unique properties of gold nanoparticles were unknowingly utilized centuries before we even began to understand them [27]. It wasn't until 1857, when Michael Faraday discovered that washing gold films produced a ruby-colored liquid, that we got a first scientific description of gold colloids [28, 29]. Almost half a century later, in 1898, Richard Adolf Zsigmondy developed another synthesis method to produce colloidal gold in diluted solution [30]. He combined this method with Faraday's to devise a two-step method based on nucleation, an approach that would later be rediscovered and further developed into what is now called seed-mediated synthesis (see Section 3.1.3) [31]. Zsigmondy's work on colloids would eventually award him the Nobel prize in Chemistry in 1925 [32].

In 1951, John Turkevich developed a method of synthesizing gold nanoparticles through the reduction of gold ions. He investigated various approaches, such as the introduction of carbon monoxide gas into a solution of chloroauric acid and creating an electrical arc between two gold rods in a diluted solution of sodium hydroxide (Bredig's arc method [33, 34]). He also evaluated several reduction agents, but what would finally come to be known as the Turkevich method utilizes reduction by citrate [35, 36].[1] This method was further refined by G. Frens in 1972 [37] to produce more monodisperse and spherical particles with a tunable size. The details of the Turkevich method, as well as how AuNPs were synthesized for the work in this thesis, will be discussed further in Sections 3.1.1 and 4.1.

With straightforward and easily implementable methods for synthesizing AuNPs, in combination with unique and highly diverse properties and great versatility, AuNPs have become a cornerstone in numerous fields. These properties and various applications will be explored in the following section.

[1] While Turkevich et al. have been given the credit for this method, they actually adapted the method from Ernst A. Hauser and J. Edward Lynn, referring to their textbook *Experiments in Colloid Chemistry, published in 1940.*

Figure 2.1: Pictures of the north rose window at Notre-Dame Cathedral in Paris (left) and the Lycurgus cup at the British Museum in London (right). Without detailed knowledge of their properties, the colors of both of these objects were achieved by addition of gold nanoparticles. Photo to the left by Julie Anne Workman. License: CC-BY-SA 3.0. Image to the right attributed to The Trustees of the British Museum. Shared under a Creative Commons Attribution-NonCommercial-ShareAlike 4.0 International (CC BY-NC-SA 4.0) license.

2.1.1 Properties and Applications

The practical applications of AuNPs are extraordinarily extensive; from rapid antigen tests for SARS-CoV-2 [38, 39] to conductive ink in printed circuits [40], AuNPs are used in countless research fields. This is due to their many unique physical properties. To begin with, AuNPs are plasmonic (see Section 2.3.4) [11], which leads to their pronounced coloration. This is why colloidal gold appears red or purple, rather than gold-colored as some might expect. The difference in color depends on both particle size [41] and interparticle distance [22]. The distinct color of AuNPs is the property utilized in, for example, SARS-CoV-2 rapid antigen tests, in which both a test strip and AuNPs in the sensor are conjugated with target-specific antibodies [39]. As an antigen-containing sample is applied to the sensor, the antigens will bind to the AuNPs. When the sample flows through the sensor, antigens bound to AuNPs will bind to the test strip as well. The AuNPs will thereby aggregate on the strip, yielding a visible red color. Thereby, a visible test strip indicates the presence of antigens and thus a positive test. Moreover, plasmonic oscillations entail absorption of light, which is converted into heat. This can be utilized in photothermal therapy to treat, for instance, cancer tumors [42]. In such treatments, AuNPs are

conjugated to tumor-specific ligands and injected into the patient. As the AuNPs accumulate on the tumor, the tumor is irradiated with near-infrared light, which will be absorbed by the AuNPs. The absorbed energy is converted into heat increasing the temperature enough to cause cell death.

The geometry of AuNPs is moreover highly tunable. During synthesis, size and shape can easily be adjusted and surface modification techniques can be employed to adjust the functional properties of the AuNPs (see Sections 3.1.1 and 3.1.3). For instance, surface modification is utilized to conjugate antibodies to the AuNPs in both the SARS-CoV-2 antigen tests and photothermal cancer therapies, as explained above. Various target-specific ligands can be bound to the surface of AuNPs using, for instance, thiol chemistry (see Section 2.2.1) combined with click chemistry [43], to enable specific ligand attachment. Additionally, AuNPs can be modified to introduce charges [44, 45] and additional stability [46], to name just a few possibilities. One such example is the use of AuNPs to quantify matrix metalloproteinases [47], which are enzymes in the extracellular matrix that can break down proteins and have been observed to promote tumor growth [48]. The AuNPs are modified with carboxyl groups, which have high affinity for His-tags. As such, they self-assemble when mixed with peptides conjugated with hexahistidine on both ends. The self-assembly causes a detectable colorimetric shift. By designing the peptide such that it is cleaved by matrix metalloproteinases, the presence of such proteins breaks the self-assembly and thus reverses the spectral shift. Through this response, the amount of matrix metalloproteinases can be estimated.

Furthermore, AuNPs are inert as well as biocompatible and generally non-toxic (depending on e.g. particle size, dose and surface coating) making them highly useful for medical and pharmacological applications [11]. Additionally, they are strong scatterers and absorbers, which is utilized extensively in microscopy, e.g. for detection and contrast enhancement [49]. These properties are only a selection of the many advantageous properties of AuNPs, which again is why their applications are extraordinarily vast.

2.2 Surface Modification

Surface modification refers to the alteration of the surface of a material to introduce certain physical, chemical or biological properties. This process is employed extensively in, among countless other fields, biotechnology and biomedicine, as it allows for the fabrication of surfaces and particles specifically tailored for e.g. biocompatibility, target affinity and selective interaction with the environment. More mechanical surface modifications such as coatings and etching have been utilized for millenia. From the ancient Romans using opus signinum (a mixture of sand and crushed pottery) for waterproofing [50], to the development of methods for passivation of metal surfaces to prevent corrosion in the 1800s (although not fully understood until the 1960s) [51]. As methods progressed, focus started to shift from macroscopic techniques to molecular levels. In the 1980s, a crucial discovery was made, as Nuzzo and Allara demonstrated the formation of self-assembled monolayers

(SAMs) [52]. These highly organized structures spontaneously form by adsorption as an ordered monolayer on a surface [53]. The discovery of SAMs provided a revolutionary technique for molecular-level surface modification, and they have since been extensively utilized in e.g. biosensors and on nanoparticles to create chemically selective and functionally versatile surfaces [16, 54].

2.2.1 Thiol-Based Surface Modification

Thiols[2] are organosulfur compounds with the characteristic form R−SH, where R is any organic group and −SH is a sulfhydryl functional group, also known as the thiol group. A central property for the use of thiols in biological research in general, and for this thesis in particular, is the high affinity of the −SH group to certain metal surfaces, especially gold. Thiols can bind to gold surfaces by chemisorption through the sulfhydryl group. To form a covalent bond at the surface, the −SH is deprotonated, yielding a thiolate anion which binds to the gold [56]. Notably, it is yet unknown what happens to the cleaved hydrogen. It has even been suggested by Inkpen et al. [57] that SAMs formed from thiol-functionalized compounds in solution are physisorbed rather than chemisorbed, implying that the hydrogen is retained.

The high affinity of thiol to metals, especially the Au−S bond, is utilized extensively for modification of both surfaces and nanoparticles in a broad range of applications. Commonly, the thiol can be employed as an anchor between the surface and a functional unit or spacer. There are several benefits of utilizing Au−S interactions. Gold is inert and does not easily oxidize. Moreover, due to the high affinity of the Au−S bond, the anchored molecule can be equipped with other functional groups without disrupting the thiol conjugation [58]. As such, in addition to utilizing thiols as anchors of a SAM to sterically passivate a surface or nanoparticles, they can be utilized to tether molecules with specific binding affinities, such as antibodies or DNA, to gold surfaces and AuNPs, typically via a spacer molecule. An illustration of this approach is presented in Fig. 2.2.

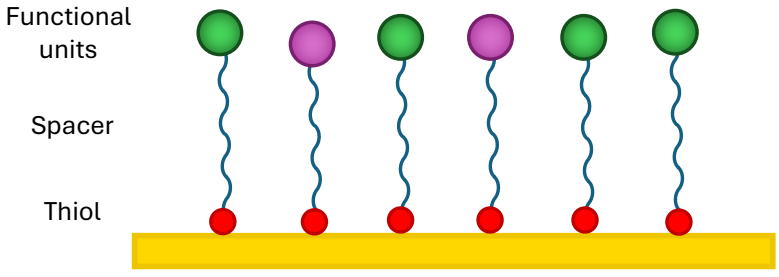

Figure 2.2: Schematic representation of the conjugation of functional units to a planar gold surface via thiol-gold interaction. The thiol is employed to tether a spacer to the surface, onto which various functional units can be conjugated.

[2]Thiols are also known as mercaptans, a historical name derived from the latin "mercurium captans" meaning "seizing mercury". This name refers to how easily thiols bind to mercury-based compounds and was introduced by William Christopher Zeise in the 1830s [55].

2.2.2 Polyethylene Glycol

Polyethylene glycol (PEG) is a polymer with an exceptionally expansive range of applications, from use in drug delivery systems [59] to cosmetics [60]. This petroleum-derived compound is easily soluble in water as well as many other solvents, such as ethanol and acetone, is nontoxic and nonvolatile, among other traits which can be imparted to other compounds through conjugation [59]. As such, PEG is used extensively in pharmaceutical and medical applications. PEG is a polyether, meaning it consists of repeating units of ethylene glycol which can be described as $H-(O-CH_2-CH_2)_n-OH$, where n is the number of units. When one end of the polymer is attached to a surface, these chain-like structures can assume two main conformations: brush, which has a more extended structure, and mushroom, which is more coiled [61]. For PEG with a molecular weight of 2 kDa, for instance, the distance between PEG molecules on a surface reportedly increases from 0.7 nm in dense brush conformation to 2.7 nm for a mushroom-brush conformation, indicating a significant impact on footprint area [62]. The conformation of PEG on a surface depends on several factors such as the PEG concentration [63] and the solvent [64, 65].

An important property for biotechnological and biomedical applications is resistance to protein adsorption. By forming a SAM of PEG with hydroxyl or methoxyl end groups, protein repellency can be introduced to the modified surface [66, 67]. Moreover, replacing the terminal hydroxyl end group with other functional groups can be used to introduce additional functionality or other specific properties to the modified surface. For instance, a carboxyl end group is negatively charged at neutral pH, and can thus introduce a charge to the particle, while modification with azide groups can facilitate click chemistry and rhodamine modification introduces fluorescence.

In this thesis, thiolated PEG (SH-PEG) was grafted to the surface of the AuNPs for two reasons. Through steric stabilization, PEG will both introduce protein-repellency, preventing non-specific interaction with other biological material, and prevent AuNP aggregation in salt buffer, in this case phosphate-buffered saline (PBS).

2.2.3 Biotin and Streptavidin

A very common ligand-receptor system used in biological research is the interaction between biotin and avidin or other avidin derivatives such as streptavidin (StrAv). Biotin, also known as vitamin B_7, is involved in various metabolic processes [68]. StrAv is a tetrameric protein purified from the bacterium *Streptomyces avidinii* [69]. While biotin is quite small with a molecular weight of 244 Da, StrAv is significantly larger at 60 kDa [70]. The interaction between biotin and StrAv has one of the highest known non-covalent affinities, with a dissociation constant $K_d \approx 10^{-14}$–10^{-16} M [69]. For the work included in this thesis, a subset of biotinylated SH-PEG was included (see Sections 3.1.4 and 4.1.3). Subsequently, StrAV was added to these PEGylated AuNPs, thereby introducing biotin affinity to the AuNP which enables

complex formation with biotinylated lipid vesicles. Such complex formation has been utilized to specifically detect lipid vesicles using twilight off-axis holographic microscopy (see Section 3.3).

2.3 Optical Theory

One of the most fundamental processes for our perception and experience of the world is the interaction between light and matter. It is the reason we can see, how the sun keeps us warm, and how plants can produce the oxygen we breathe. It is also a very complex and multifaceted process. In the following section, different aspects of light-matter interaction will be discussed.

2.3.1 Propagation of Light

Light propagating through space may be described as electromagnetic waves. Such waves can be modeled mathematically using Maxwell's equations, given as

$$\begin{aligned} \nabla \cdot \mathbf{E} &= \frac{\rho}{\varepsilon_0} \\ \nabla \cdot \mathbf{B} &= 0 \\ \nabla \times \mathbf{E} &= -\frac{\partial \mathbf{B}}{\partial t} \\ \nabla \times \mathbf{B} &= \mu_0 \left(\mathbf{J} + \varepsilon_0 \frac{\partial \mathbf{E}}{\partial t} \right), \end{aligned} \tag{2.1}$$

where $\mathbf{E}$ is the electric field, $\mathbf{B}$ is the magnetic field, ρ is the electric charge density, $\mathbf{J}$ is the current density and t is time [71]. Furthermore, the vacuum permittivity ε_0 and the vacuum permeability μ_0 are known constants. These equations, in combination with the Lorentz force, form the foundation of classical electromagnetism.

From Maxwell's equations, wave equations can be derived. In a homogeneous and transparent medium, the electromagnetic wave equation is

$$\nabla^2 \mathbf{E} = \varepsilon \mu \frac{\partial^2 \mathbf{E}}{\partial t^2}, \tag{2.2}$$

where ε and μ are the permittivity and permeability, respectively, of the medium. A particularly straightforward solution to Maxwell's equations and the wave equation is a plane wave, given as

$$\mathbf{E} = E_0 e^{-i(\mathbf{k}\cdot\mathbf{r}+\omega t)}, \tag{2.3}$$

where $E_0 = |\mathbf{E}|$ is the amplitude and ω is the angular frequency. The complex wave vector $\mathbf{k} = \mathbf{k}' + i\mathbf{k}''$ describes the propagation direction, spatial frequency and attenuation of the wave. Notably all other solutions to Maxwell's equations can be described as a superposition of plane waves [71].

So far, it has been assumed that the propagation medium does not change. However, in reality, this is seldom the case. As light travels through space it will encounter

media of different materials with varying properties, which will impact how the propagation continues, as can for instance be seen by the dependence on ε and μ in the wave equation (eq. (2.2)). A very well-known constant is the speed of light, c. As established by Maxwell's equations, the speed of light in vacuum is given by

$$c_0 = \frac{1}{\sqrt{\varepsilon_0 \mu_0}}. \tag{2.4}$$

However, as light travels in different media, the permittivity and permeability will change. Thereby, the speed of light can be described as

$$c = \frac{1}{\varepsilon \mu} = \frac{c_0}{n}, \tag{2.5}$$

where n is known as the refractive index (RI). As light propagates through the interface between two media with different RI, the propagation speed will change and consequently the propagation direction will shift towards the normal (see Fig. 2.3). This is called refraction and the change in direction can be described by Snell's law, given as

$$n_1 \sin\theta_1 = n_2 \sin\theta_2, \tag{2.6}$$

where n_i is the RI of each medium, θ_i is the angle between the propagation direction and the normal, and $i = 1, 2$ refers to each side of the interface. Propagation of light at an interface will be discussed further in Section 3.5 [72].

As will be seen in Section 2.3.4, when light travels through a medium, some of it may be absorbed. This phenomenon is included in the complex RI

$$\tilde{n} = n + i\kappa, \tag{2.7}$$

where the real part n is still the RI, describing how the light propagation is redirected by the medium, while κ is the extinction coefficient and describes how much light is absorbed [73].

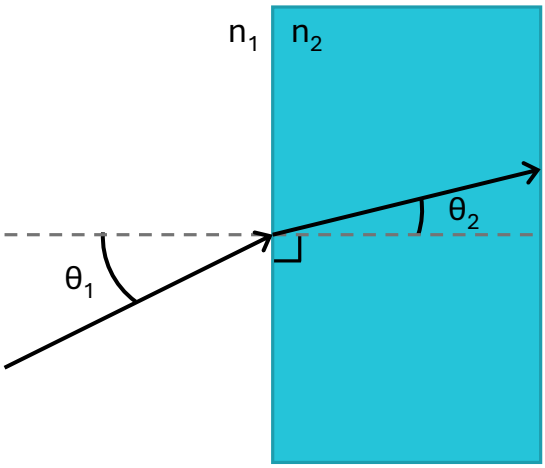

Figure 2.3: Schematic of light refraction at the interface of two materials with different refractive indices $n_1 < n_2$. Since the speed of light decreases with a higher refractive index, the propagation direction of the wave changes at the interface, bending towards the normal (dashed gray line).

2.3.2 Optical Wave Interference

As described in Section 2.3.1, propagating light can be described as a wave with a characteristic amplitude and frequency. The interference of two waves of the same frequency describes the intensity distribution of their superposition, where they will interfere either constructively, i.e. the intensities will combine, or destructively, meaning the intensities will instead cancel out, depending on their relative phase. For plane waves, the relative phase of a wave describes its relative position at any given time. If two waves are in phase, they interfere constructively. As such, it follows that the interference pattern can be utilized to evaluate the relative phase of two waves. A phase difference will develop between two initially identical waves if they propagate over different optical path lengths. Based on this, interferometers are used to evaluate differences in phase and are thus very sensitive to minute variations in path length.

In order to generate a stable interference pattern, the propagating light needs to be both spatially and temporally coherent, meaning the wave needs to maintain a consistent phase relationship over time and throughout the wavefront. For this reason, interference-based methods such as interferometry and interferometric microscopy typically utilize laser light. By the use of a beam splitter, a coherent light wave can be divided into two beams. One can be maintained as a reference, while the other can be propagated through, and interact with, a sample. The latter is often called an object beam. These beams can then be recombined, generating an interference pattern which encodes both intensity and phase information of the object beam. Thus, such information can be accessed by analyzing the interference pattern. The intensity of the interference pattern of the reference beam E_r and the object beam E_o is given by

$$I = |E_r + E_o|^2 = I_r + I_o + 2\sqrt{I_r I_o}\cos\left(\varphi_r \varphi_o\right), \tag{2.8}$$

where I_i is the intensity and φ_i is the phase of wave $i = r, o$, respectively. This is the basic principle of holography, through which the entire complex-valued optical field can be reconstructed. A specific type of holography called twilight off-axis holography will be presented in Section 2.5.

2.3.3 Scattering of Light

Light scattering occurs when matter absorbs and re-emits light in many directions. It is fundamentally caused by heterogeneities, either in the form of particles or other inhomogeneities, such as density fluctuations, in the medium [74]. These will alter certain propagation properties such as direction and, in many cases, polarization. How the light scatters depends on the relation between the size of the particle (or another heterogeneity) and the wavelength of the incident light. If the particle is much smaller than the wavelength, Rayleigh scattering will occur [72]. This is, for example, how sunlight is scattered in our atmosphere. For Rayleigh scattering, the intensity I of the unpolarized scattered light by a particle of radius r is given by

$$I = I_0 \left(\frac{1 + \cos^2\theta}{2R^2}\right)\left(\frac{2\pi}{\lambda}\right)^4 \left(\frac{m^2 - 1}{m^2 + 2}\right)^2 r^6, \tag{2.9}$$

where I_0 is the incident light intensity, R is the distance from the scattering particle, λ is the wavelength of the light, θ is the scattering angle, and r is the radius of the particle. Moreover, m is the refractive index of the particle normalized by the refractive index of the medium [75]. An important observation from this relation is that

$$I \propto \lambda^{-4}. \tag{2.10}$$

Consequently, scattering is significantly stronger for shorter wavelengths. As an aside, I would be remiss not to mention that this is why the sky appears blue. As sunlight is scattered by molecules in the atmosphere, blue light will scatter more than red, since blue light has shorter wavelengths. Another important insight is that $I \propto r^6$, which will be relevant in later sections regarding scattering-based size estimation (see Sections 3.6 and 3.7).

The scattering of particles with diameters closer to the wavelength of the incident light is not well described as Rayleigh scattering. Instead, Mie theory[3] may be utilized. This theory is the analytical solution of Maxwell's equations, assuming homogeneous, isotropic and spherical particles. Under Mie theory, the scattered intensity is an infinite sum, rather than a simple closed-form expression. Scattering can be described by the scattering cross section, which is given as

$$Q_{\text{sca}} = \frac{2}{x^2} \sum_{n=1}^{\infty} (2n+1) \left(|a_n|^2 + |b_n|^2 \right), \tag{2.11}$$

where a_n and b_n are so-called Mie coefficients [77]. These are complex functions, containing Bessel functions and resonance behavior from electromagnetic wave interactions, both in and around the particle. Q_{sca} also depends on the size parameter x, which is given as

$$x = \frac{2\pi r}{\lambda}, \tag{2.12}$$

i.e. the ratio of the, for spherical particles, radius and the wavelength of light [78]. This factor determines the size regime to which a particle belongs. If $x \ll 1$, the particle is in the Rayleigh regime, if $x \approx 1$, Mie scattering should be considered and if $x \gg 1$, geometric optics [75] may instead be utilized, although Mie theory is valid in all three regimes. For metallic particles, the size moreover affects the plasmon resonance, which will be discussed further in Section 2.3.4, and the balance between scattering and absorption. The size parameter moreover indicates the amount of light that is back scattered compared to forward scattered. For small x, scattering is symmetrical, meaning the amount of forward and backward scattering is equal. For large x, however, light is strongly scattered in the forward direction [74]. Additional particle properties such as shape, surface structure and relative RI can further impact the anisotropy of light scattering.

[3]This theory was first developed by Gustav Mie in 1908 in order to, as it happens, understand the colors of colloidal gold [76].

2.3.4 Absorption of Light

When light encounters matter, if the frequency of the light approximately corresponds to the energy levels of the electrons in that matter, the electrons can absorb the energy of the photons. The absorbed energy can either be re-emitted as the electron returns to the ground state, as discussed in Section 2.3.3, or the light will remain absorbed by the matter. The latter phenomenon is, unsurprisingly, called absorption. As light propagates through absorptive matter, continuous absorption of photon energy will cause attenuation of the electromagnetic wave, which can be observed as a gradual decrease of the light intensity. This phenomenon is called extinction and is a combination of light scattering and absorption. It can be quantified by the extinction cross section σ, given as

$$\sigma = \sigma_s + \sigma_a, \tag{2.13}$$

where σ_s and σ_a are the scattering and absorption cross sections, respectively. The cross section is a measure of the probability of a certain interaction, such as scattering or absorption.

Since the light frequency needs to be at or near the energy levels of the electrons, the wavelength of absorbed light is specific to the matter of interest. Moreover, as more matter allows for increased light absorption, the level of absorption is dependent on matter density. These two principles are the basis of absorption spectroscopy. In principle, a sample of, typically, suspended analytes is irradiated by monochromatic light. As the wavelength of the incoming light is incrementally varied, the amount of absorbed light will increase as the frequency coincides with the energy levels of the analyte. By analyzing the absorption spectrum, material properties of the analyte can be deduced. Moreover, under certain assumptions, such as noninteracting analytes and the absence of nonlinear optical processes, the attenuation of light, i.e. absorbance, is linearly dependent on the analyte concentration. This is known as the Beer-Lambert law, or Beer's law, which states that

$$A = \log_{10}\left(\frac{I_0}{I}\right) = \varepsilon c l, \tag{2.14}$$

where A is the absorbance, I_0 is the incident light, I is the transmitted light, ε is the molar absorption coefficient, l is the optical path length and c is the concentration [79]. The molar absorption coefficient is moreover related to the extinction cross section as

$$\varepsilon = \frac{N_a}{\ln 10}\sigma, \tag{2.15}$$

where $N_\mathrm{A} = 6.022 \times 10^{23}$ mol^{-1} is the Avogadro constant. The application of absorption spectroscopy will be discussed further in Section 3.8 [74].

In addition to absorption through the excitation of individual electrons, metals are able to absorb photon energy through more complex, collective means. A defining feature of metals is a collective cloud of delocalized electrons, which is the basis of many distinguishing properties such as high thermal and electrical conductivity. At

the interface between a metal and a dielectric, a wave can be excited in this cloud, typically using light, meaning the electron density oscillates at a specific frequency. These collective oscillations are called surface plasmons and can be divided into two types: surface plasmon polaritons and localized surface plasmons. The former refers to non-radiative electromagnetic waves coupled to surface plasmons which propagate along the interface, while the latter is the localized mode which occurs in metallic nanoparticles[4]. A practical application of plasmons will be discussed in Section 3.5 [74].

2.4 Brownian Motion

Named after the Scottish botanist Robert Brown, Brownian motion is the random, jittery movement of particles suspended in a fluid [82]. In 1827, when studying plant pollen in water, Brown observed that plant cell organelles ejected from the pollen displayed a continuous trembling motion [83]. He then observed the same behavior in inorganic particles, thereby excluding any biological process behind the movement. In 1905, Albert Einstein published his seminal article on the movement of small particles [84], in which his explanation of Brownian motion provided sufficient evidence of the existence of atoms.

Einstein hypothesized that Brownian motion occurs due to constant collisions between the particle and molecules in the suspension fluid, and that this could be described by a probabilistic model. From this, he showed that the motion of Brownian particles can be described by the diffusion equation as

$$\frac{\partial \rho}{\partial t} = D\frac{\partial^2 \rho}{\partial x^2}, \tag{2.16}$$

where ρ is the number density of the particles and D is the diffusion constant, i.e. in accordance with Fick's second law of diffusion

$$\frac{\partial c(x,t)}{\partial t} = D\frac{\partial^2 c(x,t)}{\partial x^2}. \tag{2.17}$$

Here, $c(x,t)$ is the particle concentration and the equation describes the net flux of particles from regions of high concentration to regions of low concentration, which leads to a uniform particle distribution. The solution of this equation, describing the probability of locating a particle at a given position x and time t, is

$$c(x,t) = \frac{1}{\sqrt{4\pi D t}} \exp\left(-\frac{x^2}{4\pi D}\right). \tag{2.18}$$

From the time-dependent standard deviation, this Gaussian probability distribution yields the mean square displacement

$$\left\langle x^2 \right\rangle = 2Dt. \tag{2.19}$$

[4]Localized surface plasmon resonance is the phenomenon responsible for the color in church windows and the Lycurgus cup, as discussed in Section 2.1. As such, localized surface plasmon resonance has been utilized since at least the 4th century [80], but it wasn't understood properly until the 1960s [81]

Additionally, Einstein's work utilized statistical physics to relate the diffusion constant D to other physical quantities. He remarked that Brownian particles can be considered as large molecules and thus, assuming the particles don't interact, a population of such particles can be regarded as an ideal gas. Based on this assumption, he derived the Einstein relation[5], expressed as

$$D = \mu k_{\mathrm{B}} T. \tag{2.20}$$

Here, μ is the mobility, $k_{\mathrm{B}} = 1.380649 \times 10^{-23}$ J/K is the Boltzmann constant and T is the temperature of the medium. The mobility is the ratio of the terminal drift velocity of the particle and an applied external force F. Using Stokes' law, this relation can be related to the size of the particles. Since the Brownian particles are significantly bigger than the surrounding particles, the applied force is assumed to be a frictional force. Assuming spherical particles with a hydrodynamic radius r_H, this is given through Stokes' law as

$$F = 6\pi\eta r_{\mathrm{H}}, \tag{2.21}$$

where η is the viscosity of the fluid. Combining Stokes' law with the Einstein relation results in the Stokes-Einstein equation[6], which states that

$$D = \frac{k_{\mathrm{B}} T}{6\pi\eta r_{\mathrm{H}}}. \tag{2.22}$$

A combination of eqs. (2.19) and (2.22) yields a relation between the mean square displacement and the hydrodynamic radius, via the diffusion coefficient. Note that Einstein's derivation was made in one dimension. In three dimensions, the diffusion equation generalizes to

$$\frac{\partial \rho(\mathbf{r}, t)}{\partial t} = D\nabla^2 \rho(\mathbf{r}, t), \tag{2.23}$$

where $\mathbf{r} = (x, y, z)$ and $\rho(\mathbf{r}, t)$ is the probability distribution in three-dimensional space. From this, the mean square displacement in three dimensions is related to diffusion as

$$\left\langle r^2 \right\rangle = \left\langle x^2 + y^2 + z^2 \right\rangle = 6Dt. \tag{2.24}$$

As the Stokes-Einstein equation does not depend on dimensionality, it remains the same in three-dimensional space.

The relation between the mean square displacement and hydrodynamic radius is the basis of diffusion-based particle size estimation, which allows for estimations of particles below the optical resolution limit. In this thesis, this has been utilized for nanoparticle tracking analysis (Section 3.7), dynamic light scattering (Section 3.6) and twilight off-axis holographic microscopy (Section 3.3). An important aspect to consider when utilizing particle tracking to estimate the mean square displacement is

[5] This relation was actually discovered several times independently. First by William Sutherland in 1904, then by Einstein in 1905 and lastly by Marian Smoluchowski in 1906. It is not clear why the relation was named after Einstein specifically[85].

[6] Also known as the Stokes-Einstein-Sutherland equation.

the position uncertainty, caused both by limitations of the position estimation of the tracking software and the particle movement during exposure time. It should moreover be noted that the hydrodynamic radius is not strictly identical to the physical size of the particle. The hydrodynamic radius, also known as the Stokes radius, is the size of a hard, solid and spherical particle with the same diffusion coefficient. As such, for analytes which deviate from these assumptions, e.g. non-spherical macromolecules, the estimated hydrodynamic radius may correspond poorly to the actual size of the analyte.

2.5 Twilight Off-Axis Holography

Holographic microscopy is an interferometric imaging technique that allows for the complete reconstruction of an electromagnetic wavefront. Through the use of optical imaging theory, Fourier analysis and interference between a reference beam and an object beam (see Section 2.3.2), the full complex-valued optical field can be reconstructed. From this, both the real and imaginary parts of the optical field can be quantified. This allows for a more comprehensive characterization of the light scattered by the sample compared to techniques limited to the real part of the signal. Specifically, evaluation of the real and imaginary parts of the field can be used to distinguish between metallic and dielectric particles, as will be discussed in Section 2.5.1 [86].

One particular variation of holographic microcopy is off-axis holography. Off-axis here refers to the offset angle at which the reference and object beams are recombined. A schematic of an off-axis holographic microscope is presented in Fig. 2.4a. Assuming the reference beam is a plane wave at an angle θ against the propagation direction of the object beam, the intensity of two interfering beams is given by

$$I = |E_r|^2 + |E_o|^2 + E_o^*|E_r|e^{-ik\sin\theta} + E_o|E_r|e^{ik\sin\theta}, \tag{2.25}$$

where E_r and E_o are the amplitude of the reference beam and object beam, respectively, and k is the magnitude of the wave vector. Here, $*$ denotes the complex conjugate defined such that if $z = A\exp(i\theta)$, then $z^* = A\exp(-i\theta)$, where $A \in \mathbb{R}$. The interference gives rise to a sinusoidal interference pattern, which can be described by three spatial frequencies, specifically

$$\begin{aligned} \nu_0 &= 0 \\ \nu_1 &= \frac{k\sin\theta}{2\pi} \\ \nu_2 &= -\frac{k\sin\theta}{2\pi}. \end{aligned} \tag{2.26}$$

These signals can be isolated in the frequency domain, meaning the interferometric parts of the measured signal can be quantified separately from the intensity terms through Fourier transform.

In order to detect scattered light in the object beam, the scattered light must be

sufficiently intense relative to the non-scattered background. Therefore, the limit of detection is determined by the signal-to-background ratio. Given this, the detection limit can be lowered by introducing a low-frequency attenuation filter (LFAF), i.e. a semi-transparent optical filter situated in the Fourier plane of a 4f system, consisting of two lenses separated by two focal lengths, which will both Fourier transform the incoming signal. As the object beam reaches the first lens of the system, the background signal propagates as a plane wave, while the scattered light has been deflected by the sample. Since the Fourier transform of a plane wave is approximately a point, and vice versa, by placing the LFAF in the Fourier plane, the background signal can be selectively attenuated while the scattered object beam is left mostly unaffected. Thus, the scattered intensity can be increased without altering the background, thereby increasing the signal-to-background ratio as well. This principle is illustrated in Fig. 2.4b.

2.5.1 Scattering and Absorption of the Optical Field

A significant advantage of utilizing off-axis holography, compared to e.g. intensity-based methods, is the ability to reconstruct the complex-valued optical field, allowing both the real and imaginary parts of the signal to be analyzed. These parts relate to different aspects of light-matter interaction. As demonstrated in ref. [87] (as well as in Paper I), the real part of the optical field for particles fulfilling $|E_p| \ll 1$, where E_p is the particle signal, is related to the intensity I such that to a first approximation, attenuation of light is given by

$$\Delta I \propto 2\mathrm{Re}(E_p). \tag{2.27}$$

It is here apparent that the real part of the complex optical signal is related to light attenuation, which in turn stems from absorption (see Section 2.3.4). For a nanoparticle with extinction cross section σ, the integrated real part is given as

$$\iint \mathrm{Re}(E_p)\ \mathrm{d}A \approx -\frac{\sigma}{2}. \tag{2.28}$$

Furthermore, ref. [87] also shows that the imaginary part of the signal, given the same assumptions as above, is approximately equal to the phase shift. Since the phase shift is related to the wavelength λ, as well as the particle volume V and relative refractive index Δn, i.e. the difference in refractive index between the particle and the medium, it follows that the integrated imaginary part of the optical field is given as

$$\iint \mathrm{Im}(E_p)\ \mathrm{d}A \approx \frac{2\pi}{\lambda} V \Delta n. \tag{2.29}$$

Given these relations between light-matter interaction and the complex-valued optical field, it follows that since light interaction with metallic nanoparticles (below a certain size) is dominated by absorption, while dielectric particles mainly scatter light, evaluation of the real and imaginary parts of the signal can be utilized to distinguish material properties. This distinction is the basis of the use of twilight off-axis holographic microscopy for the specific detection of biological particles, as will be presented in Section 3.3.

Note that the specifics of this reasoning only applies when the difference in refractive index between the particle and the surrounding medium is much smaller than 1. For a more comprehensive derivation of these relations via the complex polarizability, see ref. [88].

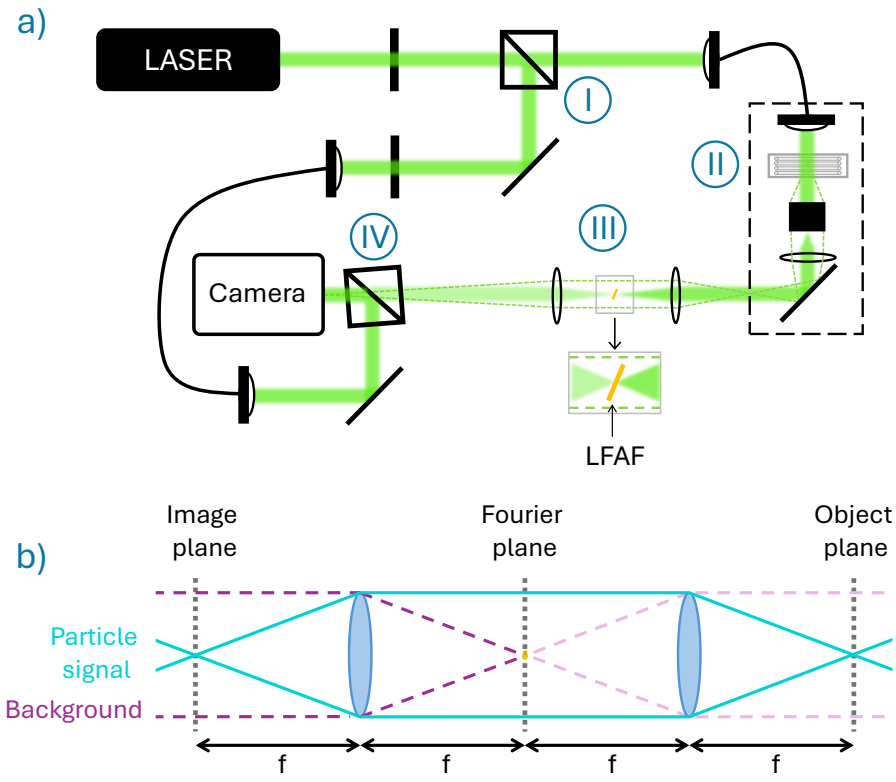

Figure 2.4: a) Schematic illustration of a twilight off-axis holographic microscope. Laser light is separated into two by a polarizing beam splitter (I). The object beam is passed through the sample (II) and a 4f system with a low-frequency attenuation filter at the Fourier plane (III) before being recombined with the reference beam at an offset angle (IV) by the camera. **b)** Illustrative explanation of how the low-frequency attenuation filter functions. Two lenses are placed with a double focal length's separation, with the filter placed between them in the Fourier plane. The first lens Fourier transforms the incoming image, and the filter in the Fourier plane attenuates the background signal selectively before the second lens Fourier transforms the signal back into an image.

3
Experimental Methods

The following chapter outlines the methods employed in this thesis, including the synthesis of materials, their subsequent characterization, and the experimental techniques used. Details of sample preparations and other experimental procedures are presented in Chapter 4.

3.1 Gold Nanoparticles

While AuNPs, both surface-modified and bare, are available commercially, for the purposes of this thesis AuNPs have instead been synthesized and functionalized in-house. This was done in order to carefully control the number of ligands on the particle surface, as well as to reduce the amount of detectable debris in the sample.

3.1.1 Synthesis

AuNPs can be synthesized by a variety of methods. An outline of a typical procedure is presented in Fig. 3.1. Essentially, the process encompasses the following components and steps:

1. Gold precursor
2. Reduction
3. Nucleation and growth
4. Stabilization

Let us examine these one by one.

Gold Precursor
Gold precursors are gold in a soluble form, typically containing gold in an oxidized state such as Au^{3+} and Au^{1+}. These serve as the starting material of the gold nanoparticles. Commonly used gold precursors include gold(III) chloride hydrate ($HAuCl_4$), also known as chloroauric acid, and sodium tetrachloroaurate ($NaAuCl_4$) [89]. In this thesis, chloroauric acid has been used. This inorganic compound is synthesized by dissolving gold in aqua regia, which is a mixture of concentrated nitric acid and hydrochloric acid [90]. The solution is then evaporated carefully, leaving a yellow powder.

Reduction
In order to form AuNPs from the oxidized Au in the precursors, the ions need to be reduced. Thus, a reduction agent is introduced which donates electrons to the

gold ion, thereby producing Au^0. In addition to investigating alternative methods, Turkevich et al. (see Section 2.1) investigated several reduction agents, such as acetone and oxalic acid, but finally arrived at citrate, which came to be known as the Turkevich method. In addition to Turkevich's work, countless methods have been investigated and developed. In recent years, a great deal of attention has been directed toward green synthesis of AuNPs. Such methods utilize non-harmful reduction agents such as bacteria, fungi and algae [91] instead of more established reduction agents which are often harmful and may be carcinogenic or otherwise toxic [92].

Nucleation and Growth

When the reduction agent is introduced to the gold precursor, the gold ions are reduced into gold atoms. Eventually, the gold atoms will reach supersaturation, i.e. a concentration higher than the equilibrium solubility limit. Such a state is thermodynamically unstable, leading to clustering of the gold atoms to return to equilibrium. This process is called nucleation. While nuclei form spontaneously at supersaturation, only nuclei above a certain critical radius will remain stable, while smaller nuclei will redissolve. Through attractive van der Waals forces, free gold atoms and smaller, unstable nuclei will cluster to the stable nuclei, making them grow. As gold atoms cluster, the supersaturation will decrease and eventually, as saturation is reached, nucleation will seize. This nucleation process can occur in one of two ways: burst or continuous nucleation. Burst nucleation refers to nucleation that occurs rapidly in a very quick "burst", followed by a pure growth phase. Nucleation thus occurs only once as the gold precursor and reduction agent are mixed. This generally leads to more monodisperse particles. For burst nucleation to occur, a strong and highly concentrated reduction agent is required. Continuous nucleation, on the other hand, entails a slower and more gradual nucleation phase where nucleation and growth overlap. This leads to a wider size distribution and occurs when weaker reduction agents are utilized. Continuous nucleation generally produces a higher AuNP yield due to the prolonged nucleation phase [93].

During the particle growth phase, instead of clustering into more nuclei, the gold atoms will aggregate with already formed gold nuclei. As more gold atoms aggregate, the nuclei will grow into fully formed AuNPs. The growth rate and final size will be determined by the amount of available gold atoms. For AuNPs, the gold atoms distribute evenly across the surface of the nucleus which leads to smooth and approximately spherical particles. By introducing some type of selective surface passivation it is possible to achieve anisotropic growth as well, meaning certain surfaces grow faster than others. For instance, by utilizing cetrimonium bromide, which preferentially binds $\{100\}$[1] faces and thus allows elongation along $\{111\}$ faces, gold nanorods can be synthesized [94].

[1] This notation, called Miller indices, is used to specify crystal planes such that each number is the reciprocal of the intercept of each plane in a unit cell. A plane that cuts the x-axis parallel to the y- and z-axes is described as (100). Moreover, using braces encompasses all planes which are symmetrically equivalent. For instance, all faces of a cube can be described as {100} due to cubic symmetry.

Stabilization
Due to their large area-to-volume ratio and high surface energy, AuNPs are generally not stable. The atoms on the surface of the particle are not fully bonded, unlike the ones in bulk, which is energetically unfavorable. In the absence of stabilizing forces, attractive van der Waals forces will cause the particles to aggregate, reducing the total surface area and lowering the surface energy [95]. As such, the AuNPs need to be stabilized. This can be achieved using various strategies. Electrostatic stabilization, for instance, refers to charged compounds aggregating on the surface of the AuNPs, causing a repulsive force between them. Such methods can be sensitive to pH levels and ionic strength. Steric stabilization uses long-chain organic molecules to introduce a physical barrier between the AuNPs. Such barriers are less sensitive to changes in pH and ionic strength [96, 97].

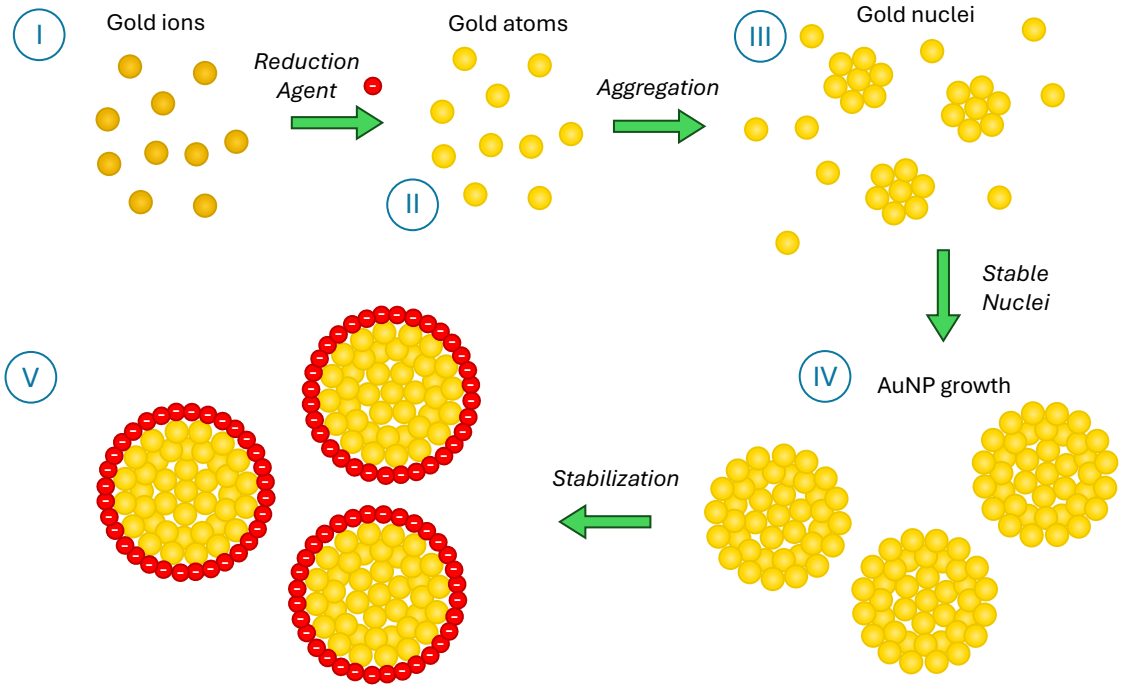

Figure 3.1: Schematic illustration of a typical AuNP fabrication procedure. A gold precursor is dissolved, resulting in suspended gold ions (I). As a reduction agent is introduced, the ions are reduced to gold atoms (II), which will aggregate by van der Waals forces, forming nanosized nuclei (III). Sufficiently large nuclei remain stable, and remaining gold atoms will cluster to the surface of such nuclei, increasing their size (IV). Finally, the remaining reduction agent aggregates on the surface of the AuNPs, forming a negatively charged layer which stabilizes the AuNPs electrostatically (V).

3.1.2 The Turkevich Method

For the work presented in this thesis, AuNPs were synthesized using the Turkevich method. This approach, as developed by John Turkevich [35] and further refined by

G. Frens [37] (see Section 2.1), is based on burst nucleation and utilizes electrostatic stabilization. Specifically, the gold precursor chloroauric acid is dissolved in water and brought to the boil. Under vigorous stirring, sodium citrate ($Na_3C_6H_5O_7$) is quickly added. As the sodium citrate and chloroauric acid are mixed, the gold ions will rapidly be reduced to gold atoms and nucleation will occur almost instantaneously, followed by a growth phase. This can be observed as a rapid change in color, from clear to almost black and then ruby red. The final size of the AuNPs will depend on the amount of chloroauric acid, as well as the temperature and pH level. Lastly, the remaining citrate ions will adsorb onto the surface of the AuNPs, creating a layer of negative charge, which introduces a repulsion force between the AuNPs, thereby preventing aggregation.

3.1.3 Seed-Mediated Synthesis

While the Turkevich method is a straightforward and reliable method to generate uniform and tunable AuNPs, it has some limitations. Principally, it only produces high-quality particles at diameters below ~ 50 nm. Above this level, the particles tend to exhibit a decreased uniformity in both size and shape. This can be addressed by introducing an additional synthesis step. Firstly, small AuNPs (around 10–15 nm) are fabricated using the Turkevich method, as described in Section 3.1.2. These may then be utilized as AuNP seeds, which larger AuNPs can grow from. In the seed-mediated growth phase, additional growth precursor is mixed with the AuNP seeds before the reduction agent is added. When the gold ions are reduced, the gold atoms will cluster to the AuNP seeds, thereby increasing their size while maintaining their spherical shape. Similar to the Turkevich method, the size of the AuNPs will depend on ratio between the gold precursor and AuNP seeds. If fewer seeds are added to a set amount of gold precursor, the final AuNPs will be larger, since the same amount of gold atoms will distribute over fewer particles. By considering this ratio, one can finely tune the size of the AuNPs [98].

A key issue with this approach is that while the gold atoms will indeed cluster to the AuNP seeds, there is nothing preventing them from aggregating with each other. This would yield additional small AuNPs, resulting in a bimodal AuNP distribution. This may, however, be mitigated by substituting the reduction agent. For instance, hydroquinone ($C_6H_4(OH)_2$) has a week reduction potential and is thus unable to spontaneously reduce gold ions. However, as reported by ref. [98], in the presence of AuNPs, this reduction potential will increase and gold ions can be reduced. Thus, gold atoms will only emerge in the proximity of the AuNP seeds, and thereby preferentially aggregate to the seeds rather than forming a secondary population.

This would be all well and good, if not for the secondary role of citrate in the Turkevich method. In addition to reducing the gold ions, citrate is utilized to stabilize the fully grown AuNPs. Completely replacing citrate with hydroquinone would thus generate uniform and monodisperse but unstable AuNPs. As such, a small amount of citrate is still necessary. While this still yields a secondary population of

small AuNPs, this population is negligible in quantity [98].

3.1.4 Surface Modification

As mentioned in Section 2.2, the AuNPs fabricated for the work in this thesis were modified for two reasons. First, the particles needed to be stabilized, both to reduce non-specific aggregation with dielectric material in biological media and to avoid salt-induced AuNP aggregation in buffered solution. This was achieved through PEGylation [99]. Secondly, the AuNPs were modified with StrAv via biotinylated PEG, in order to enable specific interaction with biotinylated surfaces. StrAv-biotin interaction is utilized extensively in biological research, due to their extraordinarily strong bond, specific binding and ease of modification (see Section 2.2.3). Streptavidin is moreover an exceptionally stable protein [69].

The AuNPs were modified with SH-PEG. PEG molecules were diluted in either 20% or 100% EtOH for SH-PEG and biotinylated SH-PEG, respectively, in order to ensure proper dilution and thus promote brush formation [100]. There are varying methods for grafting SH-PEG onto the surface of AuNPs. For example, one protocol recommends incubating AuNPs with SH-PEG at room temperature for 20 min, followed by 10 min of sonication and then further incubation overnight at 37°C [101]. Another option is incubation at room temperature for 2 h in a tabletop shaker at top speed [102]. Generally, incubation overnight is more than sufficient. The aim is to let ligand exchange between the SH-PEG and the citrate on the surface of the AuNPs to occur [103]. Since thiol has a strong affinity for gold, while citrate is bound relatively weakly, as SH-PEG molecules are mixed with citrate-stabilized AuNPs, they will start to replace the citrate on the surface. Higher temperatures typically increase the ligand exchange rate, thereby shortening the required incubation time. PEG is commonly added in large excess to ensure that a complete PEG layer is formed.

Although the multivalency of StrAv is beneficial for stable binding [104], it may in certain circumstances cause issues. Since StrAv is tetrameric, there is a risk that several AuNPs bind to the same StrAv. In order to avoid this, AuNPs can be added slowly to a solution of StrAv at high excess under vigorous stirring. As the AuNPs are introduced, this increases the probability of them being rapidly saturated by free StrAv, thereby preventing aggregation. The exact experimental procedure is presented in Section 4.1.3.

For both PEGylation and StrAv-conjugation, excess material was utilized. This calls for rigorous purification after each step, to ensure all free ligands are removed. One possible approach is to use centrifugation by repeatedly forming a soft pellet of surface-modified AuNPs and replacing the supernatant with clean solvent. Another option is to employ a centrifugal filter. Such devices consist of a filter device fitted with a filter membrane containing pores of a specific size. The sample is injected into the filter device, which is placed in a centrifuge tube. As the device is centrifuged, the suspension liquid, as well as any particles smaller than the pore size, will migrate

through the filter into the centrifuge tube, while larger particles will remain in the filter device. The remaining particles can thus be resuspended in clean solvent and the process is repeated until all excess material has been filtered out. This is the approach employed in this work.

3.2 Lipid Vesicles

Lipid vesicles, or liposomes[2], are spherical lipid bilayers which form through self-assembly in aqueous solution. They typically encompass an aqueous core, but can be formed to contain specific cargo as well. As such, liposomes are widely used in medicine, e.g. for drug and gene delivery [105]. While there are several methods of synthesis, a common approach is to first form a thin lipid film by evaporating a mixture of lipids using, for instance, nitrogen gas or in a vacuum. This film is then rehydrated, whereupon lipid vesicles form. These vesicles tend to have a quite broad size distribution, which is why additional steps are implemented to control the particle size. This can be done using the extrusion method, where lipid vesicles are repeatedly passed through a polycarbonate filter with a defined pore size. Other approaches include the sonication method, where multilamellar vesicles (i.e. vesicles containing multiple bilayers) are exposed to ultrasonic waves to break them apart and form unilamellar vesicles, or through mixing using microfluidics. For the work in this thesis, thin-film hydration followed by the extrusion method has been utilized [106].

An important part of liposome synthesis is the choice of lipids, as well as additional material in the bilayer or the core of the vesicle. These components will determine various properties, such as surface charge and stability. For the work in this thesis, lipid vesicles were synthesized using POPC (1-palmitoyl-2-oleoyl-sn-glycero-3-phosphocholine) and biotinylated DSPE-PEG (1,2-Distearoyl-sn-Glycero-3-Phosphoethanolamine-Polyethylene Glycol). POPC has a headgroup consisting of a phosphocoine, meaning the lipids are zwitterionic and thus neutral at physiological pH. It is moreover naturally found in eukaryotic cells and is thus biocompatible [107]. DSPE-PEG contains a PEG headgroup, which provides a stable spacer onto which biotin is anchored, thus introducing affinity for avidin and avidin derivatives. The specific composition and synthesis of these vesicles are presented in Section 4.2.

3.3 Twilight Off-Axis Holographic Microscopy

As discussed, a considerable benefit of holographic microscopy is the ability to access the entire complex-valued optical field. In Section 2.5.1, it was demonstrated that the real and imaginary parts of the optical field can be related to contributions from metallic and dielectric particles, respectively. Given this, twilight off-axis

[2]In certain contexts, distinction is made between *vesicle* and *liposome*, as the former is of natural origin and the latter synthetically produced. This distinction will not be relevant for, nor made in, this thesis.

holography may be used to distinguish between such particles, as well as aggregates of the two. As illustrated in Fig. 3.2, by plotting the real part versus the imaginary part, characteristic regions for each type of particle or particle complex will emerge. Based on this, twilight off-axis holography has here been utilized as a detection method for biological particles, as introduced in Paper I and further developed in Paper II. By mixing streptavidin-modified AuNPs (StrAv-AuNPs) with biotinylated large unilamellar lipid vesicles (biotin-LUVs), specific complexes will form. Using holographic microscopy, these aggregates, as well as detectable metallic and dielectric particles, can be distinguished. Since metal/dielectric complexes only form through specific StrAv-biotin interaction, the detection of such complexes corresponds to detection of biotin-LUVs. Furthermore, by tracking the particle diffusion and estimating the mean square displacement, the diffusion coefficient and thus the hydrodynamic radius can be estimated, in accordance with the Stokes-Einstein equation (eq. (2.22)).

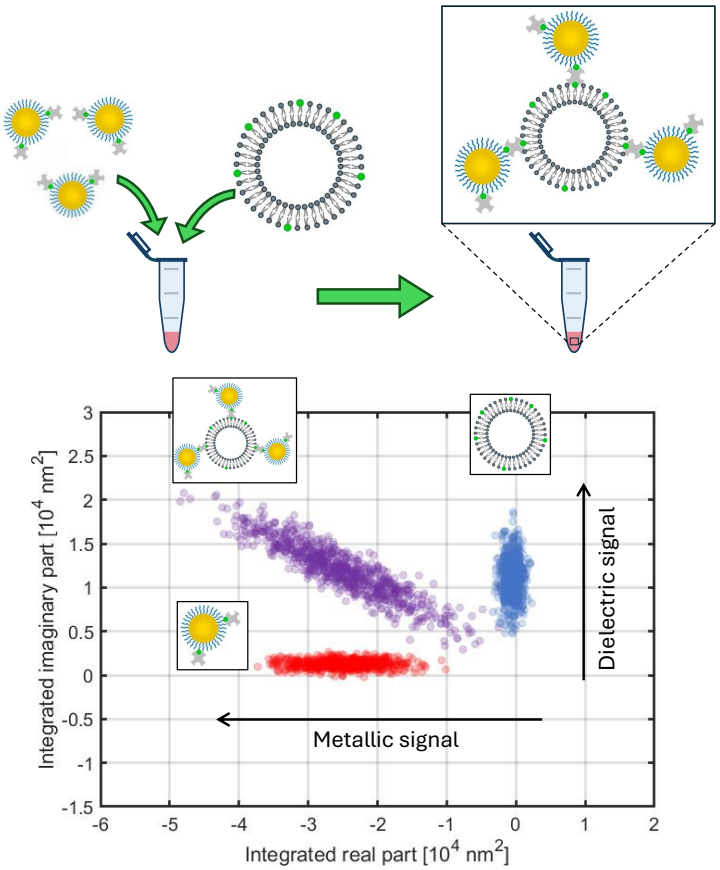

Figure 3.2: Illustration of lipid vesicle detection using twilight off-axis holographic microscopy. StrAv-AuNPs and biotin-LUVs are mixed and as they incubate together, specific StrAv-AuNP/biotin-LUV complexes will form. These are then measured using a holographic microscope. By evaluating the integrated real and imaginary parts of the signal, detected particles can be differentiated based on material properties. As StrAv-AuNP/biotin-LUV complexes are both metallic and dielectric, they generate a uniquely detectable signal, corresponding to a characteristic region in the plot.

3.4 Waveguide Scattering Microscopy

As propagating light reaches the interface between two media of different refractive index, some of it will refract (see Section 2.3.1), whereas some of it will be transmitted. However, when the RI decreases at an interface, and the incident angle is above a critical angle θ_c from the interface normal, all incoming light will reflect. This is called total internal reflection (TIR), and the critical angle is given by Snell's law (eq. (2.6)) such that

$$\theta_c = \arcsin\left(\frac{n_2}{n_1}\right). \tag{3.1}$$

Here n_1 and n_2 are the RIs on each side of the interface, such that $n_1 > n_2$. While it is indeed true that for TIR, no incoming energy can, on average, be carried across the boundary ($n_1 < n_2$), in order to satisfy boundary conditions of the electromagnetic wave function, a propagating wave is created at the boundary which has an exponentially decaying part extending across the boundary. This interface-confined wave is known as an evanescent wave and its intensity across the boundary is given by

$$I = I_0 \exp\left(-\frac{z}{\delta}\right), \tag{3.2}$$

where z denotes distance away from the interface and δ is the is the characteristic penetration depth of the evanescent wave, defined as the intensity at which point $I(z) = I_0/e$ [108]. The penetration depth is given by

$$\delta = \frac{\lambda}{4\pi\sqrt{n_2^2 \sin\theta - n_1^2}}, \tag{3.3}$$

where λ is the wavelength of the incident light in vacuum [108]. It is seen that δ is on the same order of magnitude as λ, which will typically be on the order of 100 nm. Thus, only particles close to the interface will interact with the evanescent field. Interaction kinetics can be effectively probed by studying interactions on a surface. By utilizing the limited penetration depth of an evanescent field, one can measure the scattering of light by particles bound to a surface, while unbound particles in bulk will remain outside of the field. This principle is utilized in waveguide scattering microscopy (WGSM) [72].

At a basic level, a waveguide microscope consists of three key parts: a light source, a waveguide and an objective. A waveguide chip is composed of a substrate on which a lower cladding, a core and an upper cladding is mounted. Materials are chosen such that the refractive index of the cladding is lower than that of the core. Moreover, by choosing a cladding material with a similar refractive index to that of water, one can avoid refraction at the cladding-sample interface, avoiding additional light scattering. The evanescent wave is generated by butt-coupling a single-mode optical fiber to the waveguide using a xyz-translational stage. By including a small well in the upper cladding, an injected sample can gain access to the evanescent field propagating along the core. Particles close to the surface may thus scatter light, while particles in the bulk remain outside the illumination region. Finally, an objective is placed orthogonally to the propagation direction of the incident light.

A schematic of such a setup can be seen in Fig. 3.3.

Since WGSM can be utilized for time-resolved measurement of particle binding, the rate of binding is readily estimated. Assuming diffusion-limited binding, meaning the rate of binding is controlled by how fast the particles reach the surface, the binding rate can be related to the particle concentration C by

$$\frac{\Delta c}{\Delta t} = \xi \left(D^2 Q\right)^{1/3} C, \tag{3.4}$$

where D is the diffusion constant, Q is the volumetric flow rate, and ξ is a geometry factor specified by the flow channel as

$$\xi = 0.98 \left(\frac{2}{h^2 w l}\right)^{1/3}, \tag{3.5}$$

and h, w and l are the hight width and length, repetitively, in accordance with ref. [109].

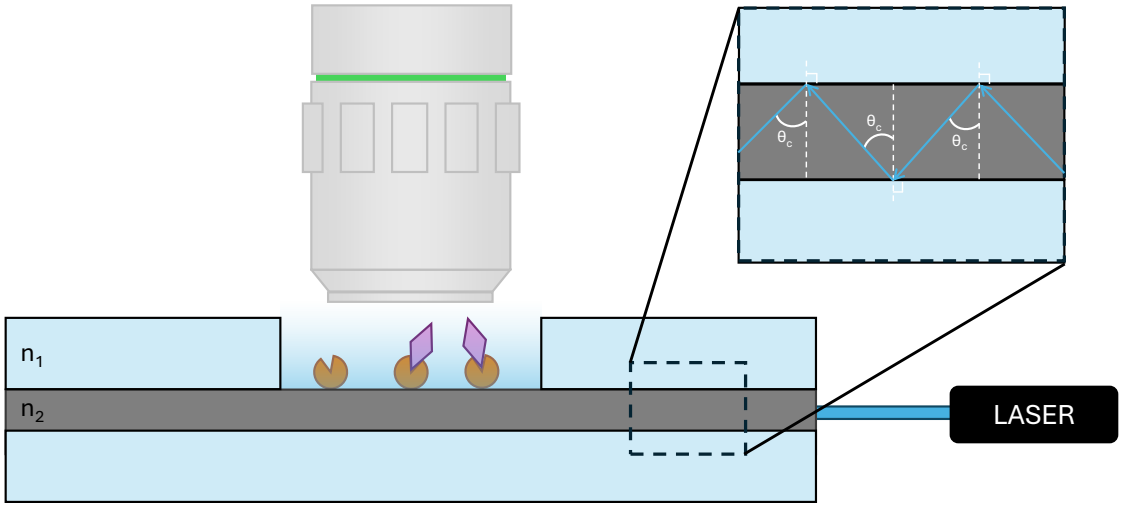

Figure 3.3: Illustrated explanation of the basic principle of waveguide scattering microscopy. Laser light is guided by an optical fiber coupled to the core of the waveguide chip such that an evanescent field is generated. Analytes are bound to the bottom of the well in the upper cladding, where the evanescent field is sufficiently intense to yield discernible scattering, which is detected by an objective mounted orthogonally against the laser propagation direction.

3.5 Surface Plasmon Resonance

As presented in Section 2.3.4, a result of the collective cloud of delocalized electrons in metals is that the energy of incident light can, under certain circumstances, excite oscillations in the electrons called plasmons. Moreover, a specific type of plasmon is the surface plasmon polariton, i.e. a non-radiative electromagnetic wave which propagates along the surface. For a photon to excite such waves, it needs to match the

surface plasmon polaritons in both frequency and momentum. Since free-space photons have less momentum than surface plasmon polaritons, coupling of photons into a surface plasmon polariton requires a coupling medium such as a prism to adjust the wave vector of the light. This allows incident light at a specific resonance angle to excite surface plasmon polaritons. Such coupling occurs under TIR conditions, meaning an evanescent field will form and excite the polaritons. This phenomenon is called surface plasmon resonance (SPR) and at this so-called SPR angle, a sharp drop in reflected light intensity, known as the SPR dip, can be detected. The surface plasmon polariton propagates at the dielectric-metal interface, partially penetrating into the dielectric medium with a distinct penetration depth. Since the evanescent field decays exponentially from the surface (see Section 3.4), the surface plasmon is highly dependent on the RI close to the surface. As such, changes of the RI, through change of medium or binding to the surface at the interface, will alter the angle of incidence required to induce SPR, and thereby the position of the SPR dip. This is utilized in SPR for biosensing, where time-resolved binding kinetics (for instance) can be probed through the change in SPR angle [76, 110].

The following describes the working principle of an SPR sensing instrument. A metal surface is irradiated by a laser through e.g. a glass prism. The incident angle is continuously varied within a set range and at a specific angle, SPR excitation will occur. This will be detected as an SPR dip. By repeating the process, time-resolved changes to the surface can be measured. A schematic of the SPR principle is shown in Fig. 3.4.

The response of an SPR measurement is the variation of the SPR angle, and is often referred to as R. This quantity can then, based on the properties of the instrument and analyte, be converted into more physically significant quantities. Since both changes of R and changes in the absorbed mass are associated with variations of the RI of the medium, the SPR response is, in accordance with ref. [111], given as

$$R = S\left(\frac{\mathrm{d}n}{\mathrm{d}C}\right) C \cdot \frac{d}{\delta} = S\left(\frac{\mathrm{d}n}{\mathrm{d}C}\right) \frac{\Gamma}{\delta}, \tag{3.6}$$

where S is the sensitivity factor of the instrument, $\mathrm{d}n/\mathrm{d}C$ is the refractive index increment of the analyte responsible for the SPR angle shift, δ is the penetration depth of the evanescent plasmon field, d is the thickness of the analyte layer (here one assumes $d \ll \delta$), and Γ is the mass coverage. The sensitivity S is given as

$$S = \frac{\Delta R}{\Delta n}, \tag{3.7}$$

where ΔR and Δn are the measured changes in response and RI after a change of medium. While ΔR can be measured directly, the change in RI can be estimated as

$$\Delta n = n_{\mathrm{prism}} \left(\sin\theta_2 - \sin\theta_1\right), \tag{3.8}$$

where n_{prism} is estimated from the SPR angle in air and $\theta_2 - \theta_1$ is the change in SPR angle after a change of medium. From this, the change in SPR angle can be

converted to mass coverage according to

$$\Gamma = \frac{\delta R}{S\left(\frac{\mathrm{d}n}{\mathrm{d}C}\right)}. \tag{3.9}$$

In this thesis, $\delta = 109$ nm has been assumed in accordance with ref. [109], and $\mathrm{d}n/\mathrm{d}C = 0.185$ mL/g is commonly used for proteins [112].

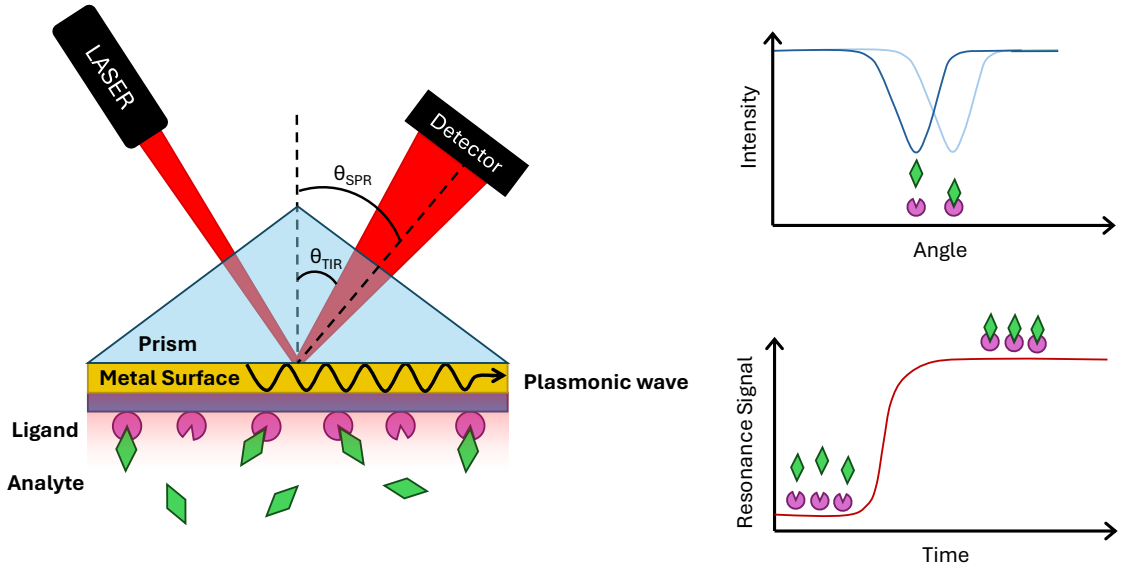

Figure 3.4: Schematic of the working principle of surface plasmon resonance (SPR). When laser light is propagated through a prism at a specific angle θ_{SPR}, the light will excite surface plasmon polaritons. As the refractive index of the surface changes, e.g. when analytes bind to surface-bound ligands, this angle will shift. Time-resolved tracking of the SPR angle can be utilized to study interaction kinetics on the surface.

3.6 Dynamic Light Scattering

Dynamic light scattering (DLS), also known as photon correlation spectroscopy or quasi-elastic light scattering, is an analysis technique based on the scattering of light and Brownian motion (see Sections 2.3.3 and 2.4). The method is primarily utilized for size estimations of suspended particles or polymers, although more sophisticated DLS setups can measure additional physical properties such as concentration and zeta potential. A sample is illuminated by a monochromatic light source, typically a laser, and then scattered by the analyte (here assumed to be suspended particles). A detector is typically placed at 173° (backscattering) or 90° (right angle), where it measures the intensity of the scattered light. As the particles move in and out of the sampling area due to Brownian motion, the intensity will fluctuate. This fluctuation is analyzed using an autocorrelation function, which is a measure of the likelihood of a particle retaining its position over time. The first-order autocorrelation function, $g^{(1)}(\tau)$ (where τ is the time delay), is the field correlation function, which describes changes in the electric field of the scattered light. The second-order autocorrelation

function, $g^{(2)}(\tau)$, is the intensity correlation function. As fluctuations of the scattered light are measured, the normalized second-order autocorrelation function is calculated as

$$g^2(\tau) = \frac{\langle I_{\text{det}}(t) \cdot I_{\text{det}}(t+\tau) \rangle}{\langle I_{\text{det}} \rangle^2}, \tag{3.10}$$

where I_{det} denotes the detected intensity and t is time. For short time delays, the correlation will be high. As the time delay increases, the correlation will decrease exponentially, until there eventually is no measurable correlation. The rate of this decrease depends on the diffusion rate of the particles. While $g^{(1)}(\tau)$ is necessary to determine particle motion, this function is typically not measured directly. However, $g^{(1)}(\tau)$ and $g^{(2)}(\tau)$ are not independent of each other. As $g^{(2)}(\tau)$ transitions from correlated to decorrelated, the interference of scattering signals from individual particles will be altered. These changes manifest in the first-order autocorrelation function. As such, $g^{(1)}(\tau)$ can be determined by measuring $g^{(2)}(\tau)$. Specifically, assuming Gaussian scattered fields with zero mean, as well as no multiple scattering, $g^{(1)}(\tau)$ and $g^{(2)}(\tau)$ are connected by the Siegert relation according to

$$g^{(2)}(\tau) = 1 + \beta |g^{(1)}(\tau)|^2, \tag{3.11}$$

where β is an instrument factor. For monodisperse particles, the electric field correlation can be expressed as a single exponential decay such that

$$g^{(1)}(\tau) = \exp(-\Gamma\tau). \tag{3.12}$$

Here, Γ is the decay rate which is related to the diffusion constant (see Section 2.4) according to

$$\Gamma = Dq^2. \tag{3.13}$$

The scattering vector q is given as

$$q = \frac{4\pi n}{\lambda} \sin\left(\frac{\theta}{2}\right), \tag{3.14}$$

where n is the RI of the solvent, λ is the wavelength of the incident light and θ is the scattering angle. It thus follows that, by extracting the diffusion factor from the autocorrelation function, and applying it to the Stokes-Einstein equation (eq. (2.22)), one can use the autocorrelation function to estimate the size distribution of the particles.[113–115].

For polydisperse samples, $g^{(1)}(\tau)$ is instead expressed as a weighted sum of exponential decays, from which particle information can be retrieved using e.g. cumulant expansion or regularization algorithms such as CONTIN. The polydispersity can moreover be quantified by the polydispersity index, which is defined as the ratio of the mass-weighted and number-weighted molecular weight and is a measure of the size heterogeneity of the samples. In addition to size distribution, this value can also be estimated from the autocorrelation function [113–115].

As mentioned, DLS is an ensemble technique, meaning the measured results are

generated from a population average. It cannot be used to estimate the size of individual particles. Consequentially, as the scattering intensity depends on the particle radius as $r^6 \propto I$, in accordance with the Rayleigh scattering principle (see eq. (2.9)), larger particles will scatter significantly more light, possibly skewing the size distribution. Note that since the scattering cross section (eq. (2.11) is inversely dependent on the size parameter (eq. (2.12)), increased scattering for larger particles holds true under Mie theory as well. However, since smaller particles scatter only minimal amounts of light, they are very difficult to detect individually. By measuring the ensemble average, DLS can be used to study particles as small as 1 nm in diameter, under optical conditions.

3.7 Nanoparticle Tracking Analysis

Nanoparticle tracking analysis (NTA) is a scattering[3] based technique that utilizes Brownian motion to estimate the particle size. Particles in suspension are illuminated by a laser and the scattered light is detected by a camera mounted perpendicular to the light path, through which the Brownian motion of the particles can be measured. As discussed in Section 2.4, the mean displacement can then be related to the diffusivity and thus the estimated hydrodynamic radius, in accordance with the Stokes-Einstein equation (see eq. (2.22)). Unlike DLS, which is an ensemble method, this approach estimates the size of each detected particle individually. As such, this method is less sensitive to polydispersity, as more intense scattering does not skew an ensemble average. However, as discussed in Section 3.6, the scattering intensity depends on particle radius as $r^6 \propto I$. Therefore, smaller particles scatter significantly less light. Since NTA is used to detect individual particles, this raises the lower bound of detectable particle sizes. While NTA struggles to detect particles close to 10 nm in diameter (depending on the refractive index of the particle [116]), DLS can be used to study particles approaching 1 nm in diameter, as mentioned in Section 3.6. Furthermore, since larger particles diffuse more slowly, it is more difficult to accurately estimate their hydrodynamic radius. They also scatter more intensely, which increases the risk of them obscuring smaller particles. Consequently, particles larger than ~ 1 µm are difficult to measure accurately [116].

Since each particle is detected individually, it is possible to estimate the particle concentration using NTA. This is done straightforwardly by simply counting the particles in the field of view and extrapolating to the full volume. As the particles diffuse in a three-dimensional fluid but are tracked in two dimensions, it is important that they don't overlap in the vertical direction. For this reason, limiting the particle concentration is key. However, in order to track enough particles to gather statistically sufficient data, the particle concentration ought not to be too low either. Given this, the recommended concentration range is 10^7–10^9 particles/ml [116].

[3]NTA setups with fluorescence modes are available as well but such methods have not been used in this work.

3.8 Ultraviolet-Visible Spectroscopy

Ultraviolet-visible Spectroscopy (UV-Vis) is a widely used analytical technique based on the absorption of light in the ultraviolet and visible region (typically around 200–800 nm). As discussed in Section 2.3.4, when absorptive molecules interact with light at specific wavelengths, they absorb light. This wavelength is dependent on the molecule and an individual molecule absorbs a certain amount of light. As such, by illuminating a sample with a spectrum of discrete wavelengths, it is possible to determine the content and concentration of the sample based on the absorbed wavelengths and maximum absorbance, respectively. This is the basic principle of UV-Vis. Essentially, the instrument consists of a light source, a monochromator and a detector. The monochromator, usually a prism or a diffraction grating, is used to select a wavelength from the broadband light source. The detector will then measure the transmitted light at that wavelength. By comparing transmitted light to the initial intensity, the absorbance is estimated. This analysis is performed over a range of discrete wavelengths, from which an absorbance spectrum can be obtained. The amount of absorbed light is dependent on the composition of the sample. In accordance with the Beer-Lambert law (eq. (2.14)), the analyte concentration can be expressed as

$$c = \frac{A}{\varepsilon l}. \tag{3.15}$$

Since the molar absorption coefficient ε and the optical path length l are typically both known constants, the concentration of an analyte can be calculated based on the measured absorbance A.

In this work, UV-Vis has been utilized to evaluate AuNPs throughout the fabrication process. In addition to calculating the particle concentration, the position of the absorbance peak can be related to the size of the AuNPs, in accordance with ref. [41]. This has been used to complement size estimations performed using DLS and NTA (see Sections 3.6 and 3.7).

4
Experimental Procedures

In the following chapter, the experimental procedures utilized in this thesis are outlined. This includes material synthesis and analytical measurements. Experimental details of all characterization methods, performed in accordance with manufacturer recommendations, are included in Paper I and Paper II.

4.1 Gold Nanoparticle Fabrication

AuNPs were produced by seed-mediated synthesis based on the Turkevich method. The particles were stabilized electrostatically by citrate before they were surface modified by addition of SH-PEG and StrAv. A schematic of the synthesis steps is shown in Fig. 4.1.

4.1.1 Seed Synthesis

To remove potential aggregates or contaminants, gold(III) chloride hydrate dissolved to a concentration of 25% w/v was centrifuged at 20370 g for 60 min at 10°C. 40 µL of the supernatant was added to 100 mL of Milli-Q water. This solution was brought to the boil on a hotplate stirrer. Under vigorous stirring, 6 mL of 1 wt% sodium citrate tribasic dihydrate was added quickly. The solution was then left at boiling point for 15 min, generating a ruby red solution of approximately 14 nm AuNP seeds.

After cooling to room temperature, the AuNPs were split into 2 mL aliquots and centrifuged at 2000 g for 30 min at 10°C. To remove any aggregates or larger AuNPs, the bottom 10% of each aliquot was discarded. The size distribution and concentration of the AuNP seeds were characterized using DLS and UV-Vis.

4.1.2 Seed-Mediated Particle Growth

Gold(III) chloride hydrate dissolved to 25% w/v was yet again centrifuged at 20370 g for 60 min at 10°C. AuNP seeds were diluted in 100 mL of Milli-Q water to a concentration of approximately 6.5×10^{10} /mL together with the top 40 µL of the centrifuged gold(III) chloride hydrate. While keeping the solution at room temperature, under rapid stirring, 1 mL of 30 mM hydroquinone and 220 µL of 1 wt% sodium citrate tribasic dihydrate was added simultaneously. The solution was left under moderate stirring for at least 60 min, producing a ruby red and slightly cloudy solution of approximately 50 nm AuNPs which were then characterized using DLS,

UV-Vis and NTA. To increase the concentration of the AuNPs, which aids in subsequent functionalization, they were centrifuged in 1 mL aliquots at 1000 g for 30 min at 10°C, forming soft extractable pellets. The concentrated solution was again characterized using DLS, UV-Vis and NTA.

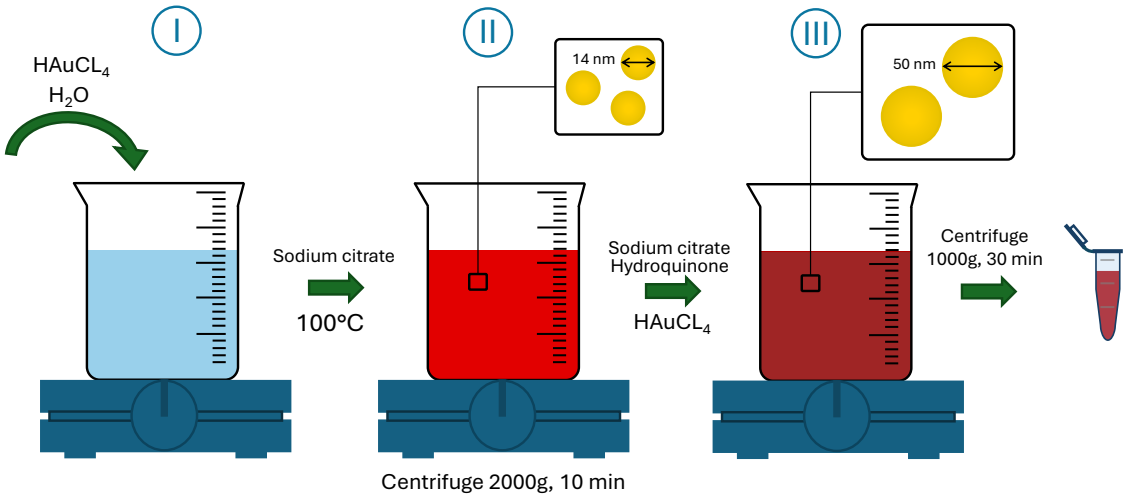

Figure 4.1: Schematic of gold nanoparticle (AuNP) fabrication. $HAuCL_4$ was added to water (I) and brought to the boil before sodium citrate (II) was added to the solution. As the gold ions were reduced, the resulting gold atoms aggregated, forming 14 nm gold seeds. More $HAuCL_4$ was added to these seeds, together with sodium citrate and hydroquinone (III), yielding approximately 50 nm AuNPs. The first centrifugation step was implemented to remove aggregates, while the latter was to increase to concentration to aid subsequent surface modification.

4.1.3 Surface Modification

The AuNPs were surface-modified in two steps. First, 3 kDa and 5 kDa SH-PEG were diluted to 10 mM in 20% EtOH and 80% Milli-Q water, while 5 kDa biotinylated SH-PEG was diluted to 10 mM in 100% EtOH. The SH-PEG was then prepared in two 250 µL mixtures of either 3 kDa or 5 kDa SH-PEG and 0.06% 5 kDa biotinylated SH-PEG at a tenfold excess over the AuNP surface area, assuming 1 nm^2 per PEG. This fraction of biotinylated PEG corresponds to approximately 5 biotin moieties per AuNP. Each solution was then mixed with 250 µL high concentration AuNPs and vortexed intensely before incubating at 4°C overnight. Excess PEG was then removed using 300 kDa centrifugal filters, centrifuged 8 times at 400 g for 17 min at 10°C.

The second surface modification step was the addition of StrAv. As previously discussed (see Section 2.2.3), StrAv has a tetrameric binding capacity to biotin. As such, the introduction of StrAv to the PEGylated AuNPs may lead to aggregation. As the aim is to saturate each biotinylated AuNP with free StrAv, aggregation was minimized by slow addition of AuNPs into an excess of StrAv moieties. AuNPs were diluted in Milli-Q water to a concentration on the order of 10^{11} /ml with 0.25 mg/ml bovine serum albumin (BSA) and, using a positive displacement pump, carefully in-

troduced at 2 µL/min to a solution of StrAv with a StrAv:Biotin ratio of 10:1, 100:1 or 1000:1, depending on the AuNP (see Section 5.2 for further details). The solution was then filtered 8 times at 400 g for 17 min at 10°C using 300 kDa centrifugal filters and stored in PBS with 0.1 mg/ml BSA.

4.2 Lipid Vesicle Synthesis

The lipid vesicles utilized in this thesis were composed of 99% POPC and 1% DSPE-PEG-Biotin. The lipids were dissolved in chloroform and mixed to a final concentration of 2 mg/mL before the chloroform was dried under a nitrogen gas flow and then left to fully evaporate in vacuum overnight. The ensuing lipid film was then rehydrated with 2 mL of PBS and vortexed for approximately 10 min. After rehydration, 1 mL of the solution was extruded 25 times through a polycarbonate membrane filter with 400 nm pores. The size distribution and particle concentration were estimated using NTA.

4.3 Measurements

The work included in this thesis mainly centers around three techniques: twilight off-axis holographic microcopy, WGSM and SPR. Details around their implementation are presented here, whereas background theory can be found in Chapter 3.

4.3.1 Twilight Off-Axis Holography

Three types of samples were prepared: StrAv-AuNPs, biotin-LUVs and StrAv-AuNPs+biotin-LUVs. Each sample was prepared with a total volume of 30 µL and the final StrAv-AuNP and biotin-LUV concentrations were 6.6×10^{10} /ml and 5×10^{8} /ml, respectively. The samples were left to incubate for 30 min at room temperature before they were pipetted into a BSA-coated microfluidic channel in the microscope. The flow rate was controlled gravitationally by manually adding PBS to the outlet. Each measurement consisted of three 1500 frame videos at 41 frames/s.

4.3.2 Waveguide Scattering Microscopy

The waveguide chip was cleaned through 5 min oxygen plasma treatment, sealed with a microfluidic channel, mounted in the microscope and then rinsed with 1% Hellmanex, Cobas and finally Milli-Q water. After rinsing with 100 µL degassed PBS at 10 µL/min, the surface was functionalized with 0.1 mg/ml PLL-g-PEG and 10% biotin by flowing the mixture at 10 µL/min for 10 min. The channel was again rinsed with 100 µL degassed PBS at the same flow rate. StrAv-AuNPs were injected at 10 µL/min for 1 min, followed by PBS at the same flow rate for 10 min in order to advance the StrAv-AuNP sample past the field of view. Videos were recorded as 300 frames at 0.5 frames/s. Between each measurement, the channel was rinsed with

PBS at 10 µL/min for approximately 10-15 min. This was repeated sequentially for all StrAv-AuNP samples, in order of increasing StrAv excess during fabrication.

4.3.3 Surface Plasmon Resonance

SPR sensor chips coated with gold were cleaned in accordance with RCA-1 cleaning protocol. 2 ml of NH_2OH was added to 10 ml of H_2O followed by 2 ml of Milli-Q water. The solution was placed on a hotplate together with a separate beaker of 14 ml Milli-Q water, both of which were heated to 75°C. The chip was placed in the cleaning solution for 15 min, then transferred to the Milli-Q water and moved from the heat. After approximately 1 h, the chip was placed in 100% EtOH for transport, and finally dried under a flow of nitrogen gas before being mounted in the SPR instrument. After rinsing with Milli-Q water (using a pre-programmed "Clean All' feature in the software), a 1 nM mixture of either 3 kDa or 5 kDa SH-PEG with 1% 5 kDa biotinylated SH-PEG was introduced at 10 µL/min for 40 minutes. Following functionalization, the channels were rinsed first with Milli-Q water and then with PBS. StrAv samples was injected sequentially at increasing concentrations (from 1.7 nM to 1.7 µM) at 20 µL/min for 5 minutes. The channels were rinsed with PBS at 20 µL/min for 10 min between each sample.

5

Summary of Results

The following sections summarize the results of the two papers on which this thesis is based. The first paper introduces the use of twilight off-axis holographic microscopy to distinguish detected particles by material properties. The second paper presents further development of this technique as an aggregation-based biosensor, focusing on the fabrication of surface-modified AuNPs to form specific aggregates with target lipid vesicles. Further details of these results are found in the appended papers.

5.1 Paper I

To investigate the possibility of distinguishing between metallic and dielectric material based on the integrated real and imaginary parts of the optical signal using twilight off-axis holographic microscopy, salt-induced complexes of 10 nm AuNPs and 300 nm silica particles were analyzed. As demonstrated in Fig. 5.1, the signal from only silica has a clearly dominating imaginary part and a negligible real part, which is consistent with pure dielectric material (Section 2.5.1). Furthermore, for mixtures of AuNPs and silica in high salt concentration, the real part of the signal increases in amplitude. As AuNPs are strong absorbers, which corresponds to the real part of the signal (Section 2.5.1), it follows that these detections are complexes of both silica and AuNPs. Moreover, since the imaginary part of the signal was largely unchanged, these complexes likely consisted of individual silica particles with numerous bound AuNPs. This interpretation is further corroborated by the estimated hydrodynamic radius of the complexes, for which the increase compared to individual silica particles aligns well with the approximate size of the AuNPs.

In addition to silica/AuNP complexes, mixtures of silica particles and AuNPs yield a second population of detections (Fig. 5.1b). Based on the dominating real part and negligible imaginary part, this population corresponds to pure AuNPs. Since the magnitude of the integrated real part is well above what is expected of individual AuNPs, these detections are most likely salt-induced AuNP aggregates. Furthermore, the number of AuNPs in these clusters can be estimated from the integrated real part using eq. (2.28) by relating the total extinction cross section to that of individual AuNPs. From this, it was concluded that the AuNP aggregates consisted of approximately 100 AuNPs. By considering these aggregates as fractal clusters with fractal dimension 2, the expected size of such clusters can be calculated. It was seen that this corresponds well with the measured hydrodynamic radius. Similarly, it was estimated using eq. (2.28) that the silica/AuNP complexes consisted of ap-

proximately 340 AuNPs/complex. Again, the hydrodynamic size of these complexes aligns well with expected values for such clusters. As such, it is concluded that by using twilight off-axis holographic microscopy, silica/AuNP complexes, pure silica particles and pure AuNPs are clearly distinguishable by quantitative differences in their real and imaginary parts, which corresponds to their material differences.

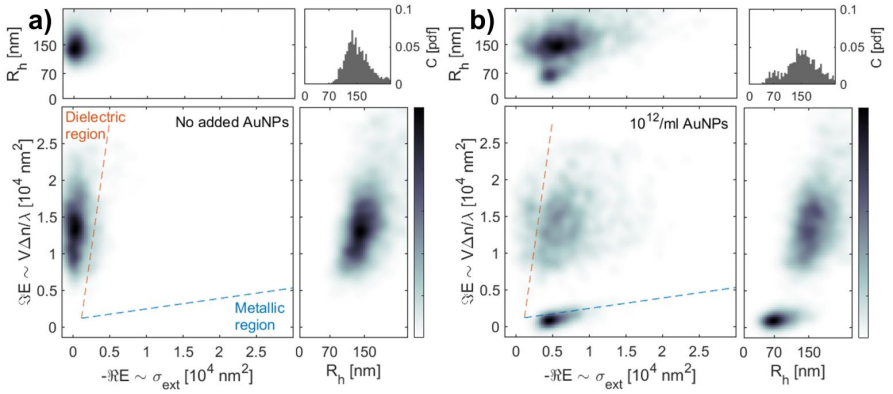

Figure 5.1: Salt-induced aggregation of silica particles and gold nanoparticles was measured using twilight off-axis holographic microscopy. Comparing the optical signal of pure silica particles **(a)** and silica particles mixed with gold nanoparticles **(b)** shows a shift towards negative values of the real part, as well as an increased concentration, for the latter, indicating aggregate formation. Moreover, the appearance of a subpopulation with low contribution from the imaginary part, a larger contribution from the real part and a hydrodynamic radius around 50-100 nm, indicates the presence of gold nanoparticle aggregates. The two dashed lines divides the plot into three regions, corresponding to dielectric, metallic and mixed particles.

To investigate whether dielectric particles significantly below the detection limit of twilight off-axis holography can be detected through aggregation with metallic particles, 50 nm StrAv-AuNPs were mixed with 200 nm biotin-LUVs (Fig. 5.2a). It was seen that the imaginary part of the signal is higher than expected for pure AuNPs, from which it can be concluded that these detections correspond to StrAv-AuNP/biotin-LUV complexes. As neither monomeric StrAv-AuNPs nor individual biotin-LUVs are detectable using this instrument, it follows that these complexes contain multiple AuNPs and biotin-LUVs. Based on the real part of the optical signal of these complexes, the average number of StrAv-AuNPs per complex ranges between 2 for the smallest complexes and 12 for the largest, and increases with the estimated hydrodynamic radius (Fig. 5.2c). Furthermore, by subtracting the hydrodynamic radius and integrated imaginary part of the StrAv-AuNPs, given that the number of StrAv-AuNPs is known by eq. (2.28), the contribution of the biotin-LUVs to the optical signal can be ascertained. From this, in accordance with eq. (2.29), an effective RI of each vesicle can be estimated, here found to be consistent with that of water-filled vesicles enclosed by a 4 nm thick lipid bilayer (Fig. 5.2d). This highlights that not only can dielectric particles below the detection limit be detected through specific aggregation with StrAv-AuNPs, quantifiable material properties of these particles can be deduced as well.

In summary, this paper demonstrates the use of twilight off-axis holographic microscopy to distinguish particles based on material properties from the real and imaginary parts of the optical signal. This has been utilized to detect nanoparticles both above and below the detection limit. These detections are moreover quantitative, wherein the RI of biotin-LUVs as well as virus particles (see paper I) below the detection limit was estimated using the optical signal.

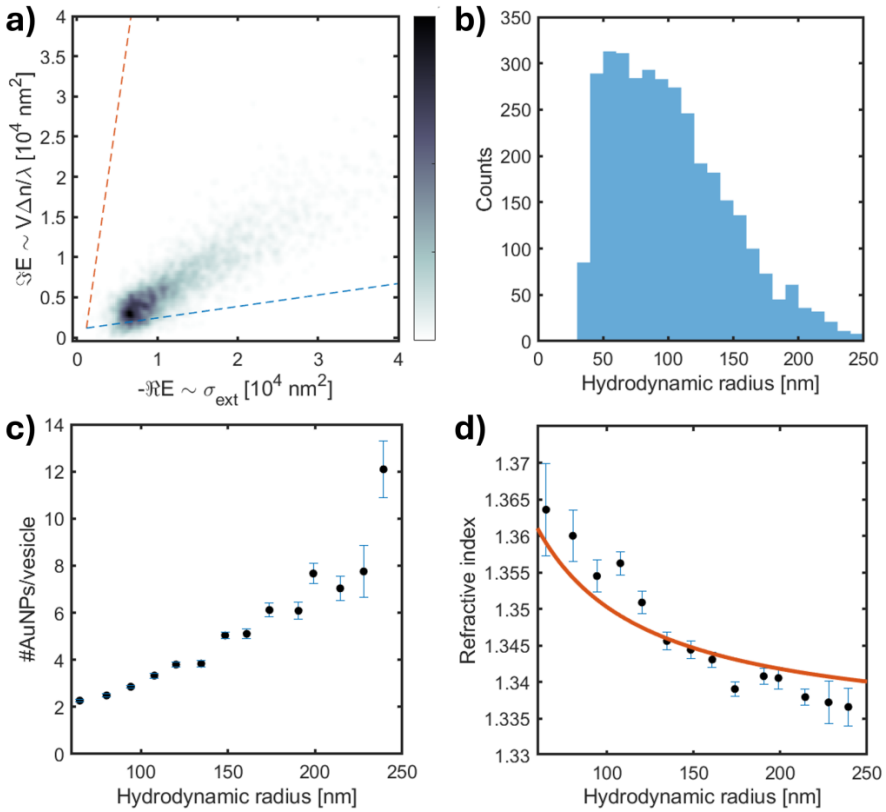

Figure 5.2: **(a)** Complexes of StrAv-AuNPs and biotin-LUVs were evaluated using twilight off-axis holographic microscopy, which showed that the complexes have a consistently higher imaginary part than expected for pure AuNPs (dashed lines indicate regions as in Fig. 5.1), which is attributed to complex formation with biotin-LUVs. **(b)** The hydrodynamic radius is moreover consistent with the size distribution measured using NTA. **(c)** The average number of StrAv-AuNPs bound per complex increases with the estimated hydrodynamic radius. **(d)** By subtracting the optical signal of the AuNPs from the total signal, the contribution of the vesicles can be isolated. From this, the RI can be estimated, which here is consistent with expected values of water-filled vesicles enclosed by a 4 nm thick lipid bilayer (solid curve).

5.2 Paper II

Having demonstrated that twilight off-axis holographic microscopy may be used to detect dielectric particles below the detection limit through aggregation with metallic nanoparticles, the aim of the following paper was to further investigate the use of StrAv-AuNPs to employ this technique as a biosensor. AuNPs were synthesized and PEGylated with a fraction of biotinylated PEG. Finally, StrAv was conjugated to the PEGylated AuNPs via biotin-binding. The StrAv-AuNPs were then mixed with biotin-LUVs. In doing so, specific StrAv-AuNP/biotin-LUV complexes were expected to form, which was evaluated using twilight off-axis holographic microscopy. As presented in Paper I (Section 5.1), StrAv-AuNPs and biotin-LUVs will contribute to the real and imaginary parts of the optical signal, respectively. It is shown in Fig. 5.3a that StrAv-AuNPs and StrAv-AUNP/biotin-LUV complexes indeed yield signals separable based on these difference in the complex-valued optical field.

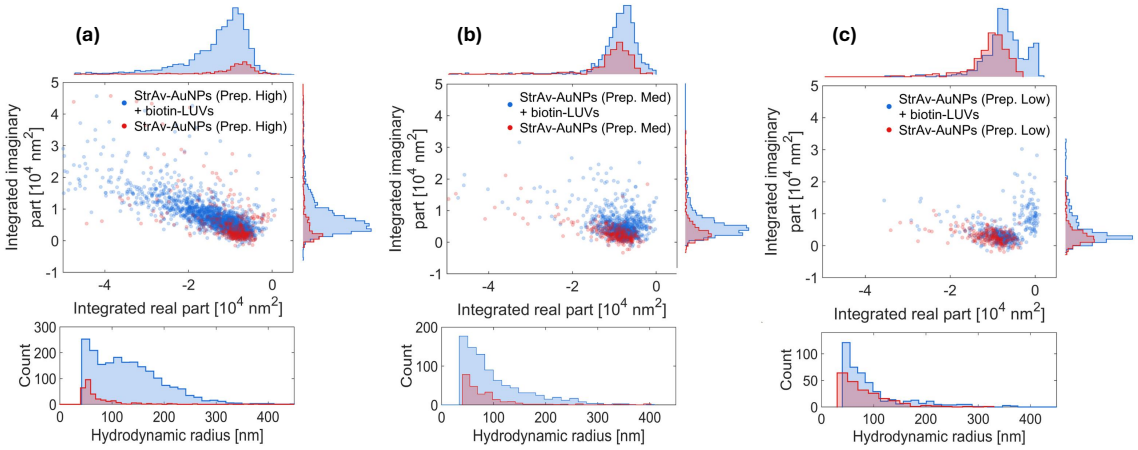

Figure 5.3: **(a)** The ability to detect biotin-LUVs through specific complex formation with StrAv-AuNPs (fabricated under high, i.e. thousandfold, StrAv excess) was evaluated using twilight off-axis holographic microscopy. Detections made for just StrAv-AuNPs (red) correspond to dimers induced by tetrameric StrAv. The increase in both the integrated real and imaginary part of the optical signal for the StrAv-AuNP/biotin-LUV mixture (blue) indicates complex formation. Moreover, decreasing the StrAv excess to a **(b)** medium (hundredfold) and **(c)** low (tenfold) StrAv excess did not alter the AuNP aggregation significantly. However, it did inhibit complex formation substantially.

As pointed out in Section 5.1, neither monomeric StrAv-AuNPs nor individual biotin-LUVs are detectable using twilight off-axis holographic microscopy, meaning the detected particles in the absence of biotin-LUVs are StrAv aggregates. Since the magnitude of the integrated real part is approximately twice that expected of an individual StrAv-AuNP, and the estimated hydrodynamic radius is consistent with dimer formation, it is concluded that these aggregates consist mainly of dimers. This aggregate formation is attributed to interlinking caused by the tetrameric biotin-binding capacity of StrAv. While the estimated concentration of these aggregates only constitutes approximately 0.01% of the total StrAv-AuNP concentration, they

still impact the ability to clearly detect and discern StrAv-AuNP/biotin-LUV complexes. As such, it is of interest to minimize the amount of StrAv-AuNP aggregation. To do so, StrAv-AuNPs were surface-modified through slow addition of PEGylated AuNPs to a high excess of StrAv. Since this still resulted in some aggregation, as seen in Fig. 5.3a, it was investigated whether the aggregation was rather a consequence of the relatively high StrAv concentration, possibly due to dynamic exchange of suspended and bound StrAv. The AuNPs were therefore similarly StrAv-modified through slow addition of AuNPs, but instead using a tenfold and hundredfold excess of StrAv over biotin. However, as demonstrated in Fig. 5.3, the amount of StrAv-AuNP aggregation was not impacted by altering the relative StrAv concentration. Instead, surprisingly, the ability to induce aggregation of StrAv-AuNPs and biotin-LUVs was significantly reduced with decreasing StrAV concentration. Specifically, under a tenfold StrAv excess, only a negligible amount of complex formation was detected, and while some complexes are seen for a hundredfold excess, clearly distinguishable StrAV-AuNP/biotin-LUV complexes are only able to form for StrAv-AuNPs fabricated with a thousandfold StrAv excess.

One plausible explanation for the lack of StrAv-AuNP/biotin-LUV complex formation is that the capacity of StrAv to bind to biotin-modified PEGylated AuNPs is insufficient at a tenfold and hundredfold StrAv excess. To investigate this possibility, all three StrAv-AuNPs were analyzed using WGSM on a surface modified with PLL-g-PEG and 10% biotin. As shown in Fig. 5.4a, the binding rate significantly decreased for StrAv-AuNPs fabricated using a lower StrAv excess, demonstrating that a higher relative StrAv concentration is necessary to yield functional StrAv-AuNPs.

Although it has previously been demonstrated that StrAv binding on a biotinylated SH-PEG surface on planar gold[1] reaches saturation within tens of minutes, such investigations often employ SH-PEG with significantly shorter chain-length [117]. This raised suspicion that PEG with a higher molecular weight may impose a steric hindrance for the StrAv to bind to the biotin embedded in the PEG layer. To investigate this hypothesis, StrAv-AuNPs were fabricated as before but the molecular weight of the non-functionalized SH-PEG was reduced from 5 kDa to 3 kDa, while the biotinylated SH-PEG remained at 5 kDa, thus potentially increasing the accessibility of the biotin. These were similarly analyzed using WGSM (Fig. 5.4b). It was observed that the binding rate increased for all three StrAv-AuNP variants, surface modified at a tenfold, hundredfold and thousandfold StrAv excess, significantly so for the StrAv-AuNPs fabricated using a lower StrAv excess which increased by a factor of 16.5 and 12.25, respectively. Moreover, the expected binding rate, based on the UV-Vis-estimated concentration, was calculated in accordance with eq. (3.4). It was estimated that the measured binding rates were, despite the extraordinarily high affinity between StrAv and biotin, an order of magnitude lower than expected, indicating reaction controlled binding which is consistent with steric hindrance. Furthermore, it is seen that the binding rate scales linearly with the

[1]Direct comparison between a planar surface and the highly curved surface of a nanoparticle should be made cautiously.

StrAv excess. This, combined with the observation of StrAv-AuNPs traversing the WGSM field of view without binding, suggests that not all StrAv-AuNPs have been successfully StrAv-modified.

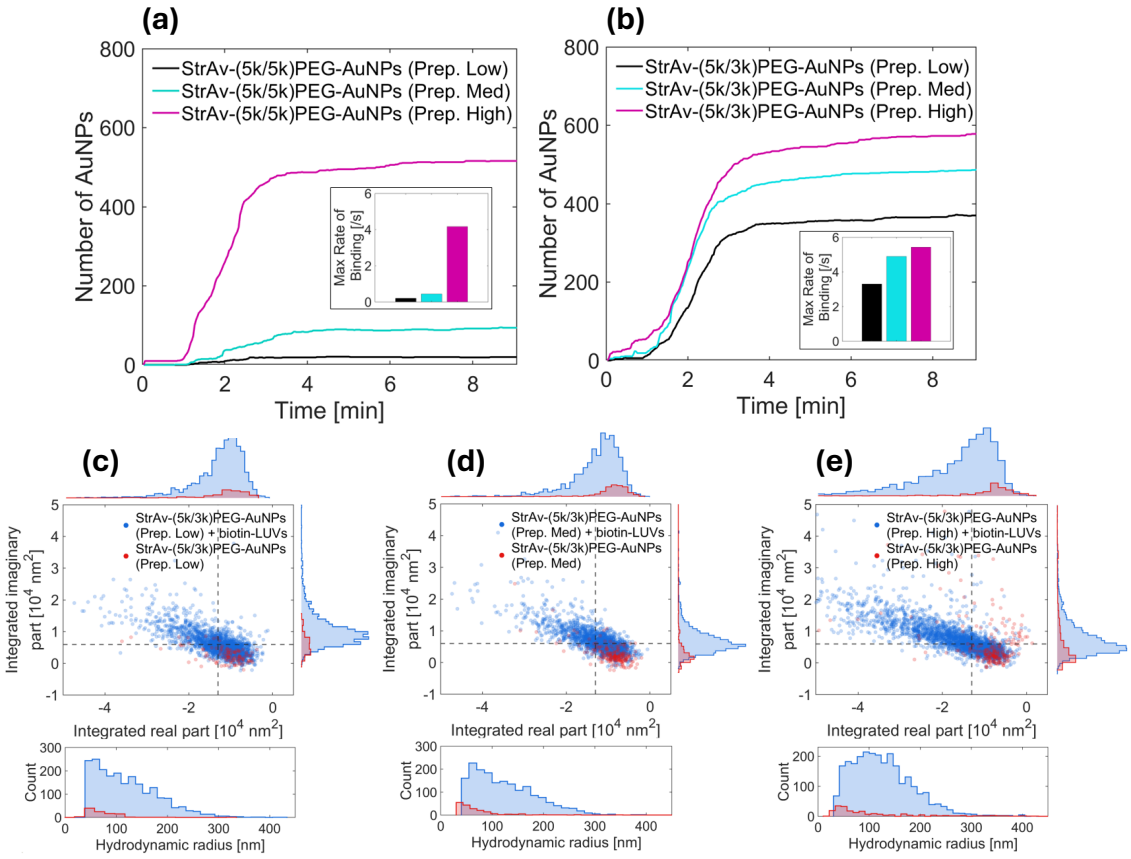

Figure 5.4: StrAv-AuNPs PEGylated with a subset of 5 kDa biotinylated SH-PEG and either **(a)** 3 kDa or **(b)** 5 kDa SH-PEG, fabricated using a low (tenfold, black), medium (hundredfold, blue) and high (thousandfold, pink) StrAv excess, were evaluated using WGSM. It is seen that decreasing the molecular weight of the non-functionalized SH-PEG, instead of using a uniform molecular weight, increases the binding rate for all three StrAv-AuNP variants. **(c-e)** StrAv-AuNPs modified using SH-PEG with reduced molecular weight were moreover evaluated using twilight off-axis holographic microscopy. While the AuNP aggregation only decreased slightly compared to Fig. 5.3, all three StrAv-AuNP variants were able to form specific complexes with biotin-LUVs. Dashed lines are used for gating to identify particle detections (see Paper II).

Finally, as StrAv-AuNPs functionalized using SH-PEG of varying molecular weight demonstrated increased binding rates on a planar biotin-modified surface, their ability to form aggregates with biotin-LUVs was evaluated using twilight off-axis holographic microscopy (Fig. 5.4). Firstly, only a slight reduction in AuNP aggregation compared to StrAv-AuNPs functionalized with SH-PEG with uniform molecular weight was observed, demonstrating that the slow addition of AuNPs into an excess StrAv suspension ensures a sufficiently high local StrAv-to-biotin ratio to minimize

aggregation. Furthermore, the twilight off-axis holography data show a distinctive increase in both the integrated real and imaginary parts, indicating that all three variants of StrAv-AuNPs form specific aggregates with, and are thus able to detect, biotin-LUVs. Thereby, the previously required excess StrAv consumption can, through this approach, be eliminated. Using this method, biotin-LUVs were detected at a sub-pM detection level.

In conclusion, the results presented in this paper show that specific binding of StrAv-AuNPs enables detection of biotin-LUVs using twilight off-axis holographic microscopy. However, PEGylating the AuNPs with functionalized and non-functionalized SH-PEG of the same molecular weight poses a steric hindrance which prevents StrAv from binding to the biotin, requiring high concentrations of StrAv to yield functional StrAv-AuNPs. Using WGSM and holographic microscopy, it was demonstrated that reducing the molecular weight of the non-functionalized SH-PEG reduced the steric hindrance, leaving the biotin more accessible for the StrAv. As the increased binding ability of the StrAv-AuNP was shown on both planar (see Paper II) and curved surfaces, these results indicate that this improvement in PEGylation strategy may be useful for a wide range of applications, including binding to cells and biological nanoparticles.

6
Outlook

In this thesis, it has been demonstrated that the ability to quantitatively distinguish between metallic and dielectric particles using twilight off-axis holographic microscopy can be utilized to detect biological targets. In Paper I, we showed that biological nanoparticles below the detection limit of twilight off-axis holography may be detected using the same technique through aggregation with AuNPs by distinguishing different material properties from the complex-valued optical field. In paper II, this method was further developed by the introduction of AuNPs functionalized for specific aggregation with the target. It was seen that PEGylation of AuNPs with uniform molecular weights appears to limit the ability of StrAv to bind to the biotinylated PEG, requiring high excess of StrAv for proper functionalization to occur. By reducing the molecular weight of the non-functionalized PEG, this issue was mitigated and functional StrAv-AuNPs could be fabricated regardless of StrAv excess. The following sections discuss how this insight may be utilized in future research.

6.1 Surface Modification of Lipid Nanoparticles

The necessity of producing functionalized nanoparticles is, of course, not limited to neither holographic microscopy nor AuNPs. One very active area of research is the surface modification of lipid nanoparticles (LNPs). LNPs are nanosized, spherical lipid structures commonly used for encapsulation and transport of biological molecules into cells [118]. These have received considerable attention in recent years, especially after their successful use in the development of mRNA vaccines for SARS-CoV-2 infection [118]. Such vaccines deliver antigen-encoding mRNA into cells, which results in production of, in this case, virus proteins which in turn stimulates the immune system to produce antibodies directed against the virus.

For this to occur, the mRNA needs to be delivered into the cytosol of the cell. As such, effective delivery systems are required. It is for this reason LNPs are used, as they are fabricated to carry genetic material as cargo, which they then transport to the intended location. While LNPs used for vaccines are taken up by cells through spontaneous adsorption of proteins on their surface, which in turn facilitates receptor-mediated uptake to a very limited subset of cells, much effort is presently invested in targeted LNP (tLNP) delivery to a wide range of different cell types for the expansion of oligonucleotide-based therapeutic applications [119]. By conjugating specific cell-targeting ligands to the LNPs, precise delivery of genetic

material can be envisioned. This is known as active targeting and can, for example, be used to increase drug concentration at the target site and deliver genetic material to specific cells. Some examples include the effective in vivo treatment of cardiac injury in mice using T cell-targeted LNPs [120], and increased uptake and cargo delivery in patient-derived leukemia cells by the use of LNPs conjugated with an antigen-specific peptide [121].

6.1.1 Quantification of Conjugated Ligands

It has been documented that the number of ligands per targeting nanoparticle substantially affects the functionality of the particle. For instance, the ligand density can be optimized for cellular uptake; while more ligands will increase the association rate, too many will cause steric hindrance [122]. Moreover, there are currently no clinically approved LNP therapies utilizing active targeting mechanisms. This is partly due to the limited availability of effective techniques to accurately quantify the number of ligands on each particle [123]. As such, advancement of such methods is a crucial aspect of the development of effective tissue-targeting LNPs for clinical use.

Estimations of ligand density on tLNPs are typically based on preparation parameters, such as the ligand-to-tLNP molar ratio, rather than direct measurement, due to inherent limitations of available measurement methods [124]. While there are some methods used for quantification of ligands on nanoparticles in general, they are not widely employed for tLNPs. These approaches are most commonly ensemble methods, which measures the total amount of attached ligands, from which the average number of ligands/particle can be estimated [125]. This is done either directly or indirectly, i.e. by either measuring the amount of conjugated ligands or by measuring the remaining amount of free ligands after functionalization. Indirect estimations are more common. Such methods include UV-Vis and colorimetric assays, while direct measurements can be performed using e.g. fluorescence-based assays. While ensemble methods are more prevalent, single-particle strategies are available. High precision does, however, remain a challenge, especially for biological nanoparticles, since only inorganic particles allow for estimations through total protein analysis [122]. Another approach is to utilize imaging methods such as transmission electron microscopy (TEM) [125]. Such methods are, nevertheless, generally complicated and often have a very low throughput. Moreover, these methods are often unsuitable for LNPs. TEM, for instance, requires a dehydration step which would likely damage the LNPs. While LNPs may be imaged using cryogenic TEM, ligand quantification would only be possible for very large ligands or using contrast agents such as AuNPs.

Recently, some potential methods for quantifying ligands on liposomes have been presented. One approach, reported by Belfiore et al [124], is to analyze liposomes with fluorescently labeled ligands using total internal reflection fluorescence microscopy. First, fluorescent ligands were immobilized on the surface of the microscope. By studying the stepwise decrease in intensity due to photobleaching, the intensity of a single fluorophore could be extrapolated. Following this, liposomes with fluorescent ligands were assessed in the same manner, allowing the fluorescent

intensity of each liposome to be translated into the number of fluorophores, and consequently ligands, on each particle. This method, however, requires the use of fluorescent labels, which may lead to potential complications. For example, accurate quantification requires complete accuracy in labeling and effective purification of free dyes. The use of florescence is moreover not applicable on LNPs designed to be applied in vivo. Additionally, the dependence on labels limits the universality of this technique, as not all ligands are susceptible to labeling. Another approach was presented by Chen et al. [123], in which they utilize nanoflow cytometry to quantify the ligand density on a single-particle level. They also employed fluorescently labeled recombinant receptors bound to the surface ligands, in order to ensure only ligands available for selective binding are included. While this high-throughput method is able to evaluate thousands or particles per minute, it also requires fluorescent labeling.

6.1.2 Ligand Density on Targeting Lipid Nanoparticles

It is apparent that effective methods for quantification of the ligand density on LNPs fabricated for active targeting is lacking. Accordingly, the primary aim of my forthcoming research is to develop a method to quantify ligand density on ligand-conjugated LNPs. In this project, our group will fabricate tLNPs modified with T cell specific nanobodies (i.e. an antigen-binding fragment of an antibody), designed to deliver CD19 CAR-coding mRNA to T cells. Specifically, the tLNPs will be surface-modified using click chemistry, which denotes an efficient, simple and highly selective approach to molecular assembly [43]. This approach is based on so-called click reactions, which are a set of reactions that fulfill certain criteria, such as modularity, high chemical yield and stereospecificity [126]. The concept was first introduced by K. Barry Sharpless et al. [127] in 2001, for which he would later jointly receive the Nobel Prize in Chemistry in 2022 with Carolyn R. Bertozzi and Morten P. Melndal [128]. While there are various click reactions, perhaps the most well-known is the copper-catalyzed reaction between an azide with an alkyne [129]. Another approach is the copper-free reaction between an azide and a reactant called dibenzocyclooctyne (DBCO) [130]. This is the approach which we plan to utilize in the upcoming project. Specifically, sortase (a bacterial enzyme) will be used to tether DBCO onto the nanobodies. This occurs through a process called sortagging, wherein the sortase cleaves the target protein at a specific site where a triglycine sequence is attached, to which the DBCO can subsequently bind [131]. Additionally, functional PEG on the LNPs will be modified with an azide end group. Thereby, a click reaction can occur between the DBCO and the azide, conjugating the nanobody to the LNP. Given the conclusions of this thesis, non-functionalized and functionalized PEG with different relative ratios and chain-lengths will be explored to precisely control conjugation efficiency.

Initially, based on the observations made in Paper II, the impact of the molecular weight ratio of functionalized and non-functionalized PEG on the efficiency of the click chemistry will be evaluated. Nanobodies will be tethered through a DBCO-azide click reaction onto PEG at varying compositions, added to a supported lipid

bilayer. Using a surface-based technique such as SPR, the attachment efficiency and saturated coverage of the nanobodies will be measured, whereby the PEG composition may be optimized. Based on this, optimally PEGylated LNPs will then be tethered onto an inert surface and, using SPR, the binding efficiency and saturated coverage of nanobodies on the LNPs will be evaluated as well. The ratio of LNP and nanobody mass may then be related to the number of nanobodies per LNP.

An additional part of this project will be to evaluate the extent to which tLNPs bind to a supported lipid bilayer modified with ectodomains of CD8, which is a receptor on T cells that controls the uptake of LNPs. This will be done using evanescent field-based microscopy, such as WGSM or total internal reflection microscopy. Under the assumption that the ligand-receptor interaction is reaction controlled, meaning the binding kinetics are limited by the association rate for the ligand-receptor interaction, it is expected that the binding rate of LNPs onto the lipid bilayer will be proportional to the number of nanobodies on the surface. As such, studying the binding kinetics may not only enable an evaluation of the specificity of the interaction but also provide additional information on the density of binding competent ligands on the tLNPs.

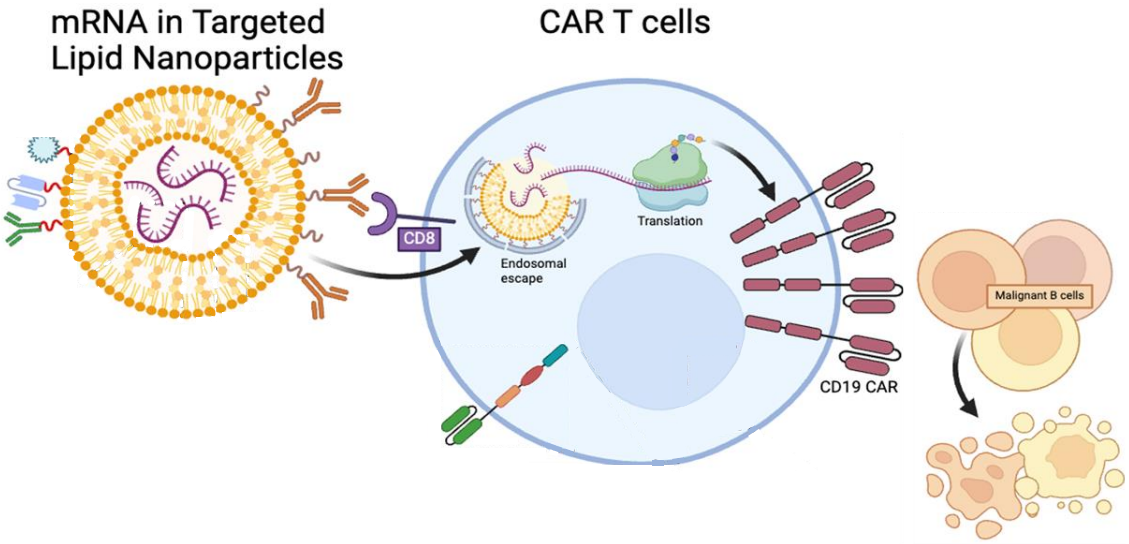

Figure 6.1: Illustration of a targeting lipid nanoparticle (tLNP) binding to a CD8 receptor in order to specifically deliver mRNA to a T cell. The purpose of the mRNA is to code for CD19 CAR (Chimeric Antigen Receptor) in order to generate CAR T cells in vivo. The aim of my future research is to evaluate the surface modification of such tLNPs.

Bibliography

[1] Robert E. Moore. An Historical Perspective on the Clinical Diagnostic Laboratory. In William B. Coleman and Gregory J. Tsongalis, editors, *Molecular Diagnostics*, pages 3–10. Humana Press, Totowa, NJ, 2006. ISBN 978-1-58829-356-5 978-1-59259-928-8. doi: 10.1385/1-59259-928-1:003. URL http://link.springer.com/10.1385/1-59259-928-1:003.

[2] Darlene Berger. A brief history of medical diagnosis and the birth of the clinical laboratory. Part 1–Ancient times through the 19th century. *MLO Med Lab Obs*, 31(7):34–40, 1999.

[3] J.A. Armstrong. Urinalysis in Western culture: A brief history. *Kidney International*, 71(5):384–387, March 2007. ISSN 00852538. doi: 10.1038/sj.ki.5002057. URL https://linkinghub.elsevier.com/retrieve/pii/S0085253815523806.

[4] H. Kenneth Walker. The Origins of the History and Physical Examination. In *Clinical Methods: The History, Physical, and Laboratory Examinations*, pages 5–21. Butterworths, Boston, 3 edition, 1990. ISBN 0-7216-8712-1.

[5] Ali Bodaghi, Nadia Fattahi, and Ali Ramazani. Biomarkers: Promising and valuable tools towards diagnosis, prognosis and treatment of Covid-19 and other diseases. *Heliyon*, 9(2):e13323, February 2023. ISSN 24058440. doi: 10.1016/j.heliyon.2023.e13323. URL https://linkinghub.elsevier.com/retrieve/pii/S2405844023005303.

[6] Nikhil Bhalla, Pawan Jolly, Nello Formisano, and Pedro Estrela. Introduction to biosensors. *Essays in Biochemistry*, 60(1):1–8, June 2016. ISSN 0071-1365, 1744-1358. doi: 10.1042/EBC20150001. URL https://portlandpress.com/essaysbiochem/article/60/1/1/78203/Introduction-to-biosensors.

[7] Miyo K Chatanaka and Eleftherios P Diamandis. Cancer biomarker concentration changes during tumor progression. *EJIFCC*, 35(3):206–209, October 2024.

[8] Allison Golden, Michelle Oliveira-Silva, Hannah Slater, Alexia Martines Vieira, Pooja Bansil, Emily Gerth-Guyette, Brandon T. Leader, Stephanie Zobrist, Alan Kennedy Braga Ferreira, Erika Crhistina Santos De Araujo, Catherine Duran De Lucena Cruz, Eduardo Garbin, Greg T. Bizilj, Sean J. Carlson, Mariana Sagalovsky, Sampa Pal, Vin Gupta, Leo Wolansky, David S. Boyle, Deusilene Souza Vieira Dall'Acqua, Felipe Gomes Naveca,

Valdinete Alves Do Nascimento, Juan Miguel Villalobos Salcedo, Paul K. Drain, Alexandre Dias Tavares Costa, Dhélio Pereira, and Gonzalo J. Domingo. Antigen concentration, viral load, and test performance for SARS-CoV-2 in multiple specimen types. *PLOS ONE*, 18(7):e0287814, July 2023. ISSN 1932-6203. doi: 10.1371/journal.pone.0287814. URL https://dx.plos.org/10.1371/journal.pone.0287814.

[9] Pavel Damborský, Juraj Švitel, and Jaroslav Katrlík. Optical biosensors. *Essays in Biochemistry*, 60(1):91–100, June 2016. ISSN 0071-1365, 1744-1358. doi: 10.1042/EBC20150010. URL https://portlandpress.com/essaysbiochem/article/60/1/91/78222/Optical-biosensors.

[10] Peter Lieberzeit, editor. *Piezoelectric Sensors*, volume 18 of *Springer Series on Chemical Sensors and Biosensors*. Springer International Publishing, Cham, 2024. ISBN 978-3-031-53784-4 978-3-031-53785-1. doi: 10.1007/978-3-031-53785-1. URL https://link.springer.com/10.1007/978-3-031-53785-1.

[11] Meiyanti Ratna Kumalasari, Rokiy Alfanaar, and Agustina Sus Andreani. Gold nanoparticles (AuNPs): A versatile material for biosensor application. *Talanta Open*, 9:100327, August 2024. ISSN 26668319. doi: 10.1016/j.talo.2024.100327. URL https://linkinghub.elsevier.com/retrieve/pii/S2666831924000419.

[12] Ricardo A. Marques Lameirinhas, Joao Paulo N. Torres, Antonio Baptista, and Maria Joao Marques Martins. A New Method to Analyse the Role of Surface Plasmon Polaritons on Dielectric-Metal Interfaces. *IEEE Photonics Journal*, 14(4):1–9, August 2022. ISSN 1943-0655, 1943-0647. doi: 10.1109/JPHOT.2022.3181967. URL https://ieeexplore.ieee.org/document/9794573/.

[13] Cheng-Ju Sung, Szu-Han Chao, and Shih-Chieh Hsu. Rapid Detection of Glucose on Nanostructured Gold Film Biosensor by Surface-Enhanced Raman Spectroscopy. *Biosensors*, 11(2):54, February 2021. ISSN 2079-6374. doi: 10.3390/bios11020054. URL https://www.mdpi.com/2079-6374/11/2/54.

[14] Yuanyuang Li, Hermann J. Schluesener, and Shunqing Xu. Gold nanoparticle-based biosensors. *Gold Bulletin*, 43(1):29–41, March 2010. ISSN 0017-1557, 2190-7579. doi: 10.1007/BF03214964. URL https://link.springer.com/10.1007/BF03214964.

[15] Lin He, Michael D. Musick, Sheila R. Nicewarner, Frank G. Salinas, Stephen J. Benkovic, Michael J. Natan, and Christine D. Keating. Colloidal Au-Enhanced Surface Plasmon Resonance for Ultrasensitive Detection of DNA Hybridization. *Journal of the American Chemical Society*, 122(38):9071–9077, September 2000. ISSN 0002-7863, 1520-5126. doi: 10.1021/ja001215b. URL https://pubs.acs.org/doi/10.1021/ja001215b.

[16] Marcio Vidotti, Rafaela F. Carvalhal, Renata K. Mendes, Danielle C. M. Ferreira, and Lauro T. Kubota. Biosensors based on gold nanostructures. *Journal of the Brazilian Chemical Society*, 22(1):3–20, Jan-

uary 2011. ISSN 0103-5053. doi: 10.1590/S0103-50532011000100002. URL http://www.scielo.br/scielo.php?script=sci_arttext&pid=S0103-50532011000100002&lng=en&nrm=iso&tlng=en.

[17] P. Yáñez-Sedeño and J. M. Pingarrón. Gold nanoparticle-based electrochemical biosensors. *Analytical and Bioanalytical Chemistry*, 382(4):884–886, June 2005. ISSN 1618-2642, 1618-2650. doi: 10.1007/s00216-005-3221-5. URL http://link.springer.com/10.1007/s00216-005-3221-5.

[18] José M. Pingarrón, Paloma Yáñez-Sedeño, and Araceli González-Cortés. Gold nanoparticle-based electrochemical biosensors. *Electrochimica Acta*, 53 (19):5848–5866, August 2008. ISSN 00134686. doi: 10.1016/j.electacta.2008.03.005. URL https://linkinghub.elsevier.com/retrieve/pii/S0013468608003599.

[19] Amit Kumar Singh, Shweta Mittal, Mangal Das, Ankur Saharia, and Manish Tiwari. Optical biosensors: a decade in review. *Alexandria Engineering Journal*, 67:673–691, March 2023. ISSN 11100168. doi: 10.1016/j.aej.2022.12.040. URL https://linkinghub.elsevier.com/retrieve/pii/S1110016822008249.

[20] H. Aldewachi, T. Chalati, M. N. Woodroofe, N. Bricklebank, B. Sharrack, and P. Gardiner. Gold nanoparticle-based colorimetric biosensors. *Nanoscale*, 10(1):18–33, 2018. ISSN 2040-3364, 2040-3372. doi: 10.1039/C7NR06367A. URL https://xlink.rsc.org/?DOI=C7NR06367A.

[21] Prashant K. Jain, Wenyu Huang, and Mostafa A. El-Sayed. On the Universal Scaling Behavior of the Distance Decay of Plasmon Coupling in Metal Nanoparticle Pairs: A Plasmon Ruler Equation. *Nano Letters*, 7(7):2080–2088, July 2007. ISSN 1530-6984, 1530-6992. doi: 10.1021/nl071008a. URL https://pubs.acs.org/doi/10.1021/nl071008a.

[22] Björn M. Reinhard, Merek Siu, Harish Agarwal, A. Paul Alivisatos, and Jan Liphardt. Calibration of Dynamic Molecular Rulers Based on Plasmon Coupling between Gold Nanoparticles. *Nano Letters*, 5(11):2246–2252, November 2005. ISSN 1530-6984, 1530-6992. doi: 10.1021/nl051592s. URL https://pubs.acs.org/doi/10.1021/nl051592s.

[23] P. Nordlander, C. Oubre, E. Prodan, K. Li, and M. I. Stockman. Plasmon Hybridization in Nanoparticle Dimers. *Nano Letters*, 4(5):899–903, May 2004. ISSN 1530-6984, 1530-6992. doi: 10.1021/nl049681c. URL https://pubs.acs.org/doi/10.1021/nl049681c.

[24] Guangyang Liu, Meng Lu, Xiaodong Huang, Tengfei Li, and Donghui Xu. Application of Gold-Nanoparticle Colorimetric Sensing to Rapid Food Safety Screening. *Sensors*, 18(12):4166, November 2018. ISSN 1424-8220. doi: 10.3390/s18124166. URL https://www.mdpi.com/1424-8220/18/12/4166.

[25] K.-H. Su, Q.-H. Wei, X. Zhang, J. J. Mock, D. R. Smith, and S. Schultz. Interparticle Coupling Effects on Plasmon Resonances of Nanogold Particles.

Nano Letters, 3(8):1087–1090, August 2003. ISSN 1530-6984, 1530-6992. doi: 10.1021/nl034197f. URL https://pubs.acs.org/doi/10.1021/nl034197f.

[26] Alexandre Aubry, Dang Yuan Lei, Stefan A. Maier, and J. B. Pendry. Interaction between Plasmonic Nanoparticles Revisited with Transformation Optics. *Physical Review Letters*, 105(23):233901, November 2010. ISSN 0031-9007, 1079-7114. doi: 10.1103/PhysRevLett.105.233901. URL https://link.aps.org/doi/10.1103/PhysRevLett.105.233901.

[27] DavidA. Giljohann, DwightS. Seferos, WestonL. Daniel, MatthewD. Massich, PinalC. Patel, and ChadA. Mirkin. Gold Nanoparticles for Biology and Medicine. *Angewandte Chemie International Edition*, 49(19):3280–3294, April 2010. ISSN 1433-7851, 1521-3773. doi: 10.1002/anie.200904359. URL https://onlinelibrary.wiley.com/doi/10.1002/anie.200904359.

[28] Michael Faraday. The Bakerian Lecture. —Experimental relations of gold (and other metals) to light. *Phil. Trans. R. Soc*, (147):145–181, 1857. doi: 10.1098/rstl.1857.0011. URL https://royalsocietypublishing.org/doi/10.1098/rstl.1857.0011.

[29] David Thompson. Michael Faraday's Recognition of Ruby Gold: the Birth of Modern Nanotechnology. *Gold Bulletin*, 40(4):267–269, 2007. doi: 10.1007/BF03215598. URL https://link.springer.com/article/10.1007/BF03215598.

[30] Richard A Zsigmondy. Properties of colloids, December 1926.

[31] Vivek Sharma, Kyoungweon Park, and Mohan Srinivasarao. Colloidal dispersion of gold nanorods: Historical background, optical properties, seed-mediated synthesis, shape separation and self-assembly. *Materials Science and Engineering: R: Reports*, 65(1-3):1–38, May 2009. ISSN 0927796X. doi: 10.1016/j.mser.2009.02.002. URL https://linkinghub.elsevier.com/retrieve/pii/S0927796X09000230.

[32] Nobel Prize Outreach 2025. Nobel Prize in Chemistry 1925, . URL https://www.nobelprize.org/prizes/chemistry/1925/summary/.

[33] H. V. Tartar and N. K. Schaffer. THE INFLUENCE OF ACIDS AND BASES ON THE INHIBITORY EFFECT OF GELATIN UPON THE CATALYTIC DECOMPOSITION OF HYDROGEN PEROXIDE BY COLLOIDAL PLATINUM. *Journal of the American Chemical Society*, 50(10):2604–2610, October 1928. ISSN 0002-7863, 1520-5126. doi: 10.1021/ja01397a003. URL https://pubs.acs.org/doi/abs/10.1021/ja01397a003.

[34] A study of ionic adsorption in solutions of silica and alumina. *Journal of the Washington Academy of Sciences*, 32(4):117–122, April 1942. URL https://www.jstor.org/stable/24531637.

[35] John Turkevich, Peter Cooper Stevenson, and James Hillier. A study of the nucleation and growth processes in the synthesis of colloidal gold. *Discussions of*

the Faraday Society, 11:55, 1951. ISSN 0366-9033. doi: 10.1039/df9511100055. URL https://xlink.rsc.org/?DOI=df9511100055.

[36] Maria Wuithschick, Alexander Birnbaum, Steffen Witte, Michael Sztucki, Ulla Vainio, Nicola Pinna, Klaus Rademann, Franziska Emmerling, Ralph Kraehnert, and Jörg Polte. Turkevich in New Robes: Key Questions Answered for the Most Common Gold Nanoparticle Synthesis. *ACS Nano*, 9(7):7052–7071, July 2015. ISSN 1936-0851, 1936-086X. doi: 10.1021/acsnano.5b01579. URL https://pubs.acs.org/doi/10.1021/acsnano.5b01579.

[37] Gerrit Frens. Controlled nucleation for the regulation of the particle size in monodisperse gold suspensions. *Nature physical science*, 241(105):20–22, January 1973. doi: 10.1038/physci241020a0.

[38] Xiao-Ling Wang, Lei Wang, Chao-Lu Hasi, Yu-Po Wang, Ajab Khan, Bin-Zhi Ren, Zhi-Zhen Liu, Shun-Lin Hou, Li-Hong Yang, Liao-Yun Zhang, Yong-Kang Dong, Jun Xu, and Jun Xie. A rapid colloidal gold immunochromatographic assay for the diagnosis of coronavirus disease 2019. *Chinese Medical Journal*, 133(16):1986–1988, August 2020. ISSN 0366-6999, 2542-5641. doi: 10.1097/CM9.0000000000000922. URL https://journals.lww.com/10.1097/CM9.0000000000000922.

[39] Sajjad Shirazi, Clark M. Stanford, and Lyndon F. Cooper. Testing for COVID-19 in dental offices. *The Journal of the American Dental Association*, 152(7): 514–525.e8, July 2021. ISSN 00028177. doi: 10.1016/j.adaj.2021.04.019. URL https://linkinghub.elsevier.com/retrieve/pii/S0002817721002762.

[40] Wenjuan Cui, Wensheng Lu, Yakun Zhang, Guanhua Lin, Tianxin Wei, and Long Jiang. Gold nanoparticle ink suitable for electric-conductive pattern fabrication using in ink-jet printing technology. *Colloids and Surfaces A: Physicochemical and Engineering Aspects*, 358(1-3):35–41, April 2010. ISSN 09277757. doi: 10.1016/j.colsurfa.2010.01.023. URL https://linkinghub.elsevier.com/retrieve/pii/S0927775710000403.

[41] Peter N. Njoki, I-Im S. Lim, Derrick Mott, Hye-Young Park, Bilal Khan, Suprav Mishra, Ravishanker Sujakumar, Jin Luo, and Chuan-Jian Zhong. Size Correlation of Optical and Spectroscopic Properties for Gold Nanoparticles. *The Journal of Physical Chemistry C*, 111(40):14664–14669, October 2007. ISSN 1932-7447, 1932-7455. doi: 10.1021/jp074902z. URL https://pubs.acs.org/doi/10.1021/jp074902z.

[42] Jeremy B. Vines, Jee-Hyun Yoon, Na-Eun Ryu, Dong-Jin Lim, and Hansoo Park. Gold Nanoparticles for Photothermal Cancer Therapy. *Frontiers in Chemistry*, 7:167, April 2019. ISSN 2296-2646. doi: 10.3389/fchem.2019.00167. URL https://www.frontiersin.org/article/10.3389/fchem.2019.00167/full.

[43] Neal K. Devaraj and M. G. Finn. Introduction: Click Chemistry. *Chemical Reviews*, 121(12):6697–6698, June 2021. ISSN 0009-2665, 1520-6890. doi:

10.1021/acs.chemrev.1c00469. URL https://pubs.acs.org/doi/10.1021/acs.chemrev.1c00469.

[44] Rakesh Gupta and Beena Rai. Effect of Size and Surface Charge of Gold Nanoparticles on their Skin Permeability: A Molecular Dynamics Study. *Scientific Reports*, 7(1):45292, March 2017. ISSN 2045-2322. doi: 10.1038/srep45292. URL https://www.nature.com/articles/srep45292.

[45] G. Tamil Selvan, Libitha Babu, Israel. M.V. Enoch, V. Srinivasadesikan, R. Mariselvam, A. Ravi Kumar, Xuesong Li, P. Jun Tang, P. Mosae Selvakumar, and Zhen Zhang. Surface-modified gold nanoparticles: A novel chemical probe for precise fluorescent detection of aluminium (Al3+) ions; investigating DFT insights and molecular logic gate behaviour. *Journal of Molecular Liquids*, 397:124039, March 2024. ISSN 01677322. doi: 10.1016/j.molliq.2024.124039. URL https://linkinghub.elsevier.com/retrieve/pii/S0167732224000941.

[46] Yubo Wang, Jose Enrico Q. Quinsaat, Tomoko Ono, Masatoshi Maeki, Manabu Tokeshi, Takuya Isono, Kenji Tajima, Toshifumi Satoh, Shin-ichiro Sato, Yutaka Miura, and Takuya Yamamoto. Enhanced dispersion stability of gold nanoparticles by the physisorption of cyclic poly(ethylene glycol). *Nature Communications*, 11(1):6089, November 2020. ISSN 2041-1723. doi: 10.1038/s41467-020-19947-8. URL https://www.nature.com/articles/s41467-020-19947-8.

[47] Gae Baik Kim, Kun Hee Kim, Yeon Hee Park, Sungho Ko, and Young-Pil Kim. Colorimetric assay of matrix metalloproteinase activity based on metal-induced self-assembly of carboxy gold nanoparticles. *Biosensors and Bioelectronics*, 41:833–839, March 2013. ISSN 09565663. doi: 10.1016/j.bios.2012.10.025. URL https://linkinghub.elsevier.com/retrieve/pii/S0956566312007002.

[48] Rajeshwar P. Verma and Corwin Hansch. Matrix metalloproteinases (MMPs): Chemical–biological functions and (Q)SARs. *Bioorganic & Medicinal Chemistry*, 15(6):2223–2268, March 2007. ISSN 09680896. doi: 10.1016/j.bmc.2007.01.011. URL https://linkinghub.elsevier.com/retrieve/pii/S0968089607000260.

[49] Yue Wu, Moustafa R.K. Ali, Kuangcai Chen, Ning Fang, and Mostafa A. El-Sayed. Gold nanoparticles in biological optical imaging. *Nano Today*, 24:120–140, February 2019. ISSN 17480132. doi: 10.1016/j.nantod.2018.12.006. URL https://linkinghub.elsevier.com/retrieve/pii/S1748013218305735.

[50] Javier Martínez Jiménez, Juan Jesús Padilla Fernández, and Elena H. Sánchez López. An Experiment Measuring Water Consumption in Roman Hydrophobic Mortar (*opus signinum*). *European Journal of Archaeology*, 27 (4):488–506, November 2024. ISSN 1461-9571, 1741-2722. doi: 10.1017/eaa.2024.20. URL https://www.cambridge.org/core/product/identifier/S1461957124000202/type/journal_article.

[51] D. D. Macdonald. Passivity–the key to our metals-based civilization. *Pure and Applied Chemistry*, 71(6):951–978, June 1999. ISSN 1365-3075, 0033-4545. doi: 10.1351/pac199971060951. URL https://www.degruyter.com/document/doi/10.1351/pac199971060951/html.

[52] Ralph G. Nuzzo and David L. Allara. Adsorption of bifunctional organic disulfides on gold surfaces. *Journal of the American Chemical Society*, 105(13): 4481–4483, June 1983. ISSN 0002-7863, 1520-5126. doi: 10.1021/ja00351a063. URL https://pubs.acs.org/doi/abs/10.1021/ja00351a063.

[53] Abraham Ulman. Formation and Structure of Self-Assembled Monolayers. *Chemical Reviews*, 96(4):1533–1554, January 1996. ISSN 0009-2665, 1520-6890. doi: 10.1021/cr9502357. URL https://pubs.acs.org/doi/10.1021/cr9502357.

[54] Elena Colangelo, Joan Comenge, David Paramelle, Martin Volk, Qiubo Chen, and Raphaël Lévy. Characterizing Self-Assembled Monolayers on Gold Nanoparticles. *Bioconjugate Chemistry*, 28(1):11–22, January 2017. ISSN 1043-1802, 1520-4812. doi: 10.1021/acs.bioconjchem.6b00587. URL https://pubs.acs.org/doi/10.1021/acs.bioconjchem.6b00587.

[55] Curt Wentrup. Zeise, Liebig, Jensen, Hückel, Dewar, and the Olefin π-Complex Bonds. *Angewandte Chemie International Edition*, 59(22):8332 – 8342, May 2020. doi: 10.1002/anie.201913840. URL https://onlinelibrary.wiley.com/doi/full/10.1002/anie.201913840.

[56] Siyam M. Ansar, Ganganath S. Perera, Dongping Jiang, Robert A. Holler, and Dongmao Zhang. Organothiols Self-Assembled onto Gold: Evidence for Deprotonation of the Sulfur-Bound Hydrogen and Charge Transfer from Thiolate. *The Journal of Physical Chemistry C*, 117(17):8793–8798, May 2013. ISSN 1932-7447, 1932-7455. doi: 10.1021/jp312836q. URL https://pubs.acs.org/doi/10.1021/jp312836q.

[57] Michael S. Inkpen, Zhen–Fei Liu, Haixing Li, Luis M. Campos, Jeffrey B. Neaton, and Latha Venkataraman. Non-chemisorbed gold–sulfur binding prevails in self-assembled monolayers. *Nature Chemistry*, 11(4):351–358, April 2019. ISSN 1755-4330, 1755-4349. doi: 10.1038/s41557-019-0216-y. URL https://www.nature.com/articles/s41557-019-0216-y.

[58] Colin D. Bain, E. Barry Troughton, Yu Tai Tao, Joseph Evall, George M. Whitesides, and Ralph G. Nuzzo. Formation of monolayer films by the spontaneous assembly of organic thiols from solution onto gold. *Journal of the American Chemical Society*, 111(1):321–335, January 1989. ISSN 0002-7863, 1520-5126. doi: 10.1021/ja00183a049. URL https://pubs.acs.org/doi/abs/10.1021/ja00183a049.

[59] Katrin Knop, Richard Hoogenboom, Dagmar Fischer, and UlrichS. Schubert. Poly(ethylene glycol) in Drug Delivery: Pros and Cons as Well as Potential Alternatives. *Angewandte Chemie International Edition*, 49(36):6288–6308,

August 2010. ISSN 1433-7851, 1521-3773. doi: 10.1002/anie.200902672. URL https://onlinelibrary.wiley.com/doi/10.1002/anie.200902672.

[60] Hyun-Jun Jang, Chan Young Shin, and Kyu-Bong Kim. Safety Evaluation of Polyethylene Glycol (PEG) Compounds for Cosmetic Use. *Toxicological Research*, 31(2):105–136, June 2015. ISSN 1976-8257. doi: 10.5487/TR.2015.31.2.105. URL https://link.springer.com/10.5487/TR.2015.31.2.105.

[61] Liwang Shi, Jinqiu Zhang, Man Zhao, Shukun Tang, Xu Cheng, Wenyuan Zhang, Wenhua Li, Xiaoying Liu, Haisheng Peng, and Qun Wang. Effects of polyethylene glycol on the surface of nanoparticles for targeted drug delivery. *Nanoscale*, 13(24):10748–10764, 2021. ISSN 2040-3364, 2040-3372. doi: 10.1039/D1NR02065J. URL https://xlink.rsc.org/?DOI=D1NR02065J.

[62] Mengyi Li, Shuai Jiang, Johanna Simon, David Paßlick, Marie-Luise Frey, Manfred Wagner, Volker Mailänder, Daniel Crespy, and Katharina Landfester. Brush Conformation of Polyethylene Glycol Determines the Stealth Effect of Nanocarriers in the Low Protein Adsorption Regime. *Nano Letters*, 21(4):1591–1598, February 2021. ISSN 1530-6984, 1530-6992. doi: 10.1021/acs.nanolett.0c03756. URL https://pubs.acs.org/doi/10.1021/acs.nanolett.0c03756.

[63] Stefan Kaufmann, Oleg Borisov, Marcus Textor, and Erik Reimhult. Mechanical properties of mushroom and brush poly(ethylene glycol)-phospholipid membranes. *Soft Matter*, 7(19):9267, 2011. ISSN 1744-683X, 1744-6848. doi: 10.1039/c1sm05746d. URL https://xlink.rsc.org/?DOI=c1sm05746d.

[64] Lokanathan Arcot, Ryosuke Ogaki, Shuai Zhang, Rikke L. Meyer, and Peter Kingshott. Optimizing the surface density of polyethylene glycol chains by grafting from binary solvent mixtures. *Applied Surface Science*, 341:134–141, June 2015. ISSN 01694332. doi: 10.1016/j.apsusc.2015.02.156. URL https://linkinghub.elsevier.com/retrieve/pii/S0169433215004833.

[65] Daniele Selli, Stefano Motta, and Cristiana Di Valentin. Impact of surface curvature, grafting density and solvent type on the PEGylation of titanium dioxide nanoparticles. *Journal of Colloid and Interface Science*, 555:519–531, November 2019. ISSN 00219797. doi: 10.1016/j.jcis.2019.07.106. URL https://linkinghub.elsevier.com/retrieve/pii/S0021979719308926.

[66] Kevin L Prime and George M Whitesides. Self-Assembled Organic Monolayers: Model Systems for Studying Adsorption of Proteins at Surfaces. *Science*, 525(5009):1164–1167, May 1991. doi: 10.1126/science.252.5009.1164. URL https://www.science.org/doi/10.1126/science.252.5009.1164.

[67] Catherine Pale-Grosdemange, Ethan S. Simon, Kevin L. Prime, and George M. Whitesides. Formation of self-assembled monolayers by chemisorption of derivatives of oligo(ethylene glycol) of structure HS(CH2)11(OCH2CH2)mOH on gold. *Journal of the American Chemical Society*, 113(1):12–20, January 1991. ISSN 0002-7863, 1520-5126. doi: 10.1021/ja00001a002. URL https://pubs.acs.org/doi/abs/10.1021/ja00001a002.

[68] Cydne A Perry and Tammy A Butterick. Biotin. *Advances in Nutrition*, 15(7): 100251, July 2024. ISSN 21618313. doi: 10.1016/j.advnut.2024.100251. URL https://linkinghub.elsevier.com/retrieve/pii/S2161831324000851.

[69] O. H. Laitinen, V. P. Hytönen, H. R. Nordlund, and M. S. Kulomaa. Genetically engineered avidins and streptavidins. *Cellular and Molecular Life Sciences*, 63(24):2992–3017, December 2006. ISSN 1420-682X, 1420-9071. doi: 10.1007/s00018-006-6288-z. URL http://link.springer.com/10.1007/s00018-006-6288-z.

[70] Shao-Chie Huang, Harold Swerdlow, and Karin D. Caldwell. Binding of biotinylated DNA to streptavidin-coated polystyrene latex: effects of chain length and particle size. *Analytical Biochemistry*, 237(1):115–122, May 1996. doi: 10.1006/abio.1996.0208. URL https://www.sciencedirect.com/science/article/pii/S0003269796902080?via%3Dihub.

[71] David K. Cheng. *Field and wave electromagnetics*. Pearson custom library. Pearson Education, pearson new international edition. edition, July 2013. ISBN 978-1-292-02656-5.

[72] B.E.A. Saleh and M.C. Teich. *Fundamentals of Photonics*. John Wiley & sons, 3 edition, August 2019. ISBN 978-0-471-83965-1.

[73] Olaf Stenzel. Linear Optical Constants I. In *Light–Matter Interaction*, pages 336–338. Springer Cham, February 2022. ISBN 978-3-030-87144-4.

[74] Craig F. Bohren and Donald R. Hurrman. *Absorption and Scattering of Light by Small Particles*. WILEY-VCH, April 1998. ISBN 978-3-527-61815-6.

[75] John H. Seinfeld and Spyros N. Pandis. *Atmospheric Chemistry and Physics*. John Wiley & Sons, 2006. ISBN 978-1-118-94740-1.

[76] Sefan Alexander Maier. *Plasmonics - Fundamentals and Applications*. Springer Science & Business Media, 2007. ISBN 978-1-4419-4113-8.

[77] A. J. Cox, Alan J. DeWeerd, and Jennifer Linden. An experiment to measure Mie and Rayleigh total scattering cross sections. *American Journal of Physics*, 70(6):620–625, June 2002. ISSN 0002-9505, 1943-2909. doi: 10.1119/1.1466815. URL https://pubs.aip.org/ajp/article/70/6/620/1040625/An-experiment-to-measure-Mie-and-Rayleigh-total.

[78] H. Hinzpeter Bakan. Scattering. In *Meteorology - Physical and Chemical Properties of the Air*, pages 145–147. Springer Materials, 4b edition, 1988. ISBN 978-3-540-31373-1.

[79] D F Swinehart. The Beer-Lambert Law. *Journal of Chemical Education*, 39 (7):333, July 1962. doi: 10.1021/ed039p333. URL https://pubs.acs.org/doi/10.1021/ed039p333.

[80] D. Barber and I. C. Freestone. An investigation of the origin of the colour of the lycurgus cup by analytical transmission electron microscopy. *Archaeometry*,

1(32):33–45, 1990. doi: 10.1111/j.1475-4754.1990.tb01079.x. URL https://onlinelibrary.wiley.com/doi/10.1111/j.1475-4754.1990.tb01079.x.

[81] Andreas Otto. Excitation of nonradiative surface plasma waves in silver by the method of frustrated total reflection. *Zeitschrift für Physik A Hadrons and nuclei*, 216(4):398–410, August 1968. ISSN 0939-7922. doi: 10.1007/BF01391532. URL http://link.springer.com/10.1007/BF01391532.

[82] Richard Feynman. The Brownian Movement. *The Feynman Lectures of Physics*, (1):41, 1964.

[83] Robert Brown. A brief account of microscopical observations made in the months of June, July and August 1827, on the particles contained in the pollen of plants; and on the general existence of active molecules in organic and inorganic bodies. *The Philosophical Magazine*, 4(21):161–173, September 1828. ISSN 1941-5850, 1941-5869. doi: 10.1080/14786442808674769. URL https://www.tandfonline.com/doi/full/10.1080/14786442808674769.

[84] A. Einstein. Über die von der molekularkinetischen Theorie der Wärme geforderte Bewegung von in ruhenden Flüssigkeiten suspendierten Teilchen. *Annalen der Physik*, 322(8):549–560, January 1905. ISSN 0003-3804, 1521-3889. doi: 10.1002/andp.19053220806. URL https://onlinelibrary.wiley.com/doi/10.1002/andp.19053220806.

[85] P. Hänggi. ROBERT BROWN AND THE POLLEN. URL https://www.physik.uni-augsburg.de/theo1/hanggi/History/Robert_Brown_Vortrag.pdf.

[86] Berenice García Rodríguez, Erik Olsén, Fredrik Skärberg, Giovanni Volpe, Fredrik Höök, and Daniel Sundås Midtvedt. Optical label-free microscopy characterization of dielectric nanoparticles. *Nanoscale*, 17(14):8336–8362, 2025. ISSN 2040-3364, 2040-3372. doi: 10.1039/D4NR03860F. URL https://xlink.rsc.org/?DOI=D4NR03860F.

[87] E Olsén. *Bridging Single-Particle Characterisation Gaps of Optical Microscopy in the Nano-Submicron Regime*. 2023. ISBN 978-91-7905-891-3.

[88] Samira Khadir, Daniel Andrén, Patrick C. Chaumet, Serge Monneret, Nicolas Bonod, Mikael Käll, Anne Sentenac, and Guillaume Baffou. Full optical characterization of single nanoparticles using quantitative phase imaging. *Optica*, 7(3):243, March 2020. ISSN 2334-2536. doi: 10.1364/OPTICA.381729. URL https://opg.optica.org/abstract.cfm?URI=optica-7-3-243.

[89] A. Alshammari, A. Köckritz, V.N. Kalevaru, and A. Martin. Influence of precursor on the particle size and stability of colloidal gold nanoparticles. In *Studies in Surface Science and Catalysis*, volume 175, pages 409–412. Elsevier, 2010. ISBN 978-0-444-53601-3. doi: 10.1016/S0167-2991(10)75072-2. URL https://linkinghub.elsevier.com/retrieve/pii/S0167299110750722.

[90] Georg Brauer. *Handbook of Preparative Inorganic Chemistry*. Academic Press, New York, 2 edition, 1963. ISBN 978-0-12-395590-6.

[91] Sundus Jabeen Amina and Bin Guo. A Review on the Synthesis and Functionalization of Gold Nanoparticles as a Drug Delivery Vehicle. *International Journal of Nanomedicine*, Volume 15:9823–9857, December 2020. ISSN 1178-2013. doi: 10.2147/IJN.S279094. URL https://pubmed.ncbi.nlm.nih.gov/33324054/.

[92] Saman Sargazi, Ushna Laraib, Simge Er, Abbas Rahdar, Mohadeseh Hassanisaadi, Muhammad Nadeem Zafar, Ana M. Díez-Pascual, and Muhammad Bilal. Application of Green Gold Nanoparticles in Cancer Therapy and Diagnosis. *Nanomaterials*, 12(7):1102, March 2022. ISSN 2079-4991. doi: 10.3390/nano12071102. URL https://www.mdpi.com/2079-4991/12/7/1102.

[93] Nguyen T. K. Thanh, N. Maclean, and S. Mahiddine. Mechanisms of Nucleation and Growth of Nanoparticles in Solution. *Chemical Reviews*, 114(15):7610–7630, August 2014. ISSN 0009-2665, 1520-6890. doi: 10.1021/cr400544s. URL https://pubs.acs.org/doi/10.1021/cr400544s.

[94] Santosh Kumar Meena and Marialore Sulpizi. Understanding the Microscopic Origin of Gold Nanoparticle Anisotropic Growth from Molecular Dynamics Simulations. *Langmuir*, 29(48):14954–14961, December 2013. ISSN 0743-7463, 1520-5827. doi: 10.1021/la403843n. URL https://pubs.acs.org/doi/10.1021/la403843n.

[95] Hoa T. Phan and Amanda J. Haes. What Does Nanoparticle Stability Mean? *The Journal of Physical Chemistry C*, 123(27):16495–16507, July 2019. ISSN 1932-7447, 1932-7455. doi: 10.1021/acs.jpcc.9b00913. URL https://pubs.acs.org/doi/10.1021/acs.jpcc.9b00913.

[96] Guozhong Cao. *Nanostructures And Nanomaterials: Synthesis, Properties And Applications*. World Scientific Publishing Company, 1 edition, April 2004. ISBN 978-1-86094-596-0.

[97] Hind Al-Johani, Edy Abou-Hamad, Abdesslem Jedidi, Cory M. Widdifield, Jasmine Viger-Gravel, Shiv Shankar Sangaru, David Gajan, Dalaver H. Anjum, Samy Ould-Chikh, Mohamed Nejib Hedhili, Andrei Gurinov, Michael J. Kelly, Mohamad El Eter, Luigi Cavallo, Lyndon Emsley, and Jean-Marie Basset. The structure and binding mode of citrate in the stabilization of gold nanoparticles. *Nature Chemistry*, 9(9):890–895, September 2017. ISSN 1755-4330, 1755-4349. doi: 10.1038/nchem.2752. URL https://www.nature.com/articles/nchem.2752.

[98] Steven D. Perrault and Warren C. W. Chan. Synthesis and Surface Modification of Highly Monodispersed, Spherical Gold Nanoparticles of 50200 nm. *Journal of the American Chemical Society*, 131(47):17042–17043, December 2009. ISSN 0002-7863, 1520-5126. doi: 10.1021/ja907069u. URL https://pubs.acs.org/doi/10.1021/ja907069u.

[99] Charitha Thambiliyagodage. Ligand exchange reactions and PEG stabilization of gold nanoparticles. *Current Research in Green and Sustainable Chem-*

istry, 5:100245, 2022. ISSN 26660865. doi: 10.1016/j.crgsc.2021.100245. URL https://linkinghub.elsevier.com/retrieve/pii/S2666086521001922.

[100] Marta Cerruti, Stefano Fissolo, Carlo Carraro, Carlo Ricciardi, Arun Majumdar, and Roya Maboudian. Poly(ethylene glycol) Monolayer Formation and Stability on Gold and Silicon Nitride Substrates. *Langmuir*, 24(19):10646–10653, October 2008. ISSN 0743-7463, 1520-5827. doi: 10.1021/la801357v. URL https://pubs.acs.org/doi/10.1021/la801357v.

[101] Nagwa El-Baz, Betty M. Nunn, Paula J. Bates, and Martin G. O'Toole. The Impact of PEGylation on Cellular Uptake and In Vivo Biodistribution of Gold Nanoparticle MRI Contrast Agents. *Bioengineering*, 9(12):766, December 2022. ISSN 2306-5354. doi: 10.3390/bioengineering9120766. URL https://www.mdpi.com/2306-5354/9/12/766.

[102] Yijia Zhang, Alice T. Liu, Yvonne R. Cornejo, Desiree Van Haute, and Jacob M. Berlin. A Systematic comparison of in vitro cell uptake and in vivo biodistribution for three classes of gold nanoparticles with saturated PEG coatings. *PLOS ONE*, 15(7):e0234916, July 2020. ISSN 1932-6203. doi: 10.1371/journal.pone.0234916. URL https://dx.plos.org/10.1371/journal.pone.0234916.

[103] Rebecca Dinkel, Björn Braunschweig, and Wolfgang Peukert. Fast and Slow Ligand Exchange at the Surface of Colloidal Gold Nanoparticles. *The Journal of Physical Chemistry C*, 120(3):1673–1682, January 2016. ISSN 1932-7447, 1932-7455. doi: 10.1021/acs.jpcc.5b11055. URL https://pubs.acs.org/doi/10.1021/acs.jpcc.5b11055.

[104] Galina V. Dubacheva, Carolina Araya-Callis, Anne Geert Volbeda, Michael Fairhead, Jeroen Codée, Mark Howarth, and Ralf P. Richter. Controlling Multivalent Binding through Surface Chemistry: Model Study on Streptavidin. *Journal of the American Chemical Society*, 139(11):4157–4167, March 2017. ISSN 0002-7863, 1520-5126. doi: 10.1021/jacs.7b00540. URL https://pubs.acs.org/doi/10.1021/jacs.7b00540.

[105] D.D. Lasic. Applications of Liposomes. In *Handbook of Biological Physics*, volume 1, pages 491–519. Elsevier, 1995. ISBN 978-0-444-81975-8. doi: 10.1016/S1383-8121(06)80027-8. URL https://linkinghub.elsevier.com/retrieve/pii/S1383812106800278.

[106] Sandy Ong, Mallikarjun Chitneni, Kah Lee, Long Ming, and Kah Yuen. Evaluation of Extrusion Technique for Nanosizing Liposomes. *Pharmaceutics*, 8 (4):36, December 2016. ISSN 1999-4923. doi: 10.3390/pharmaceutics8040036. URL https://www.mdpi.com/1999-4923/8/4/36.

[107] Lucie Huynh, Nahuel Perrot, Veronica Beswick, Véronique Rosilio, Patrick A. Curmi, Alain Sanson, and Nadège Jamin. Structural Properties of POPC Monolayers under Lateral Compression: Computer Simulations Analysis. *Langmuir*, 30(2):564–573, January 2014. ISSN 0743-7463, 1520-5827. doi: 10.1021/la4043809. URL https://pubs.acs.org/doi/10.1021/la4043809.

[108] Mario Bertolotti, Concita Sibilia, and Angela M. Guzman. *Evanescent Waves in Optics: An Introduction to Plasmonics*, volume 206 of *Springer Series in Optical Sciences*. Springer International Publishing, Cham, 2017. ISBN 978-3-319-61260-7 978-3-319-61261-4. doi: 10.1007/978-3-319-61261-4. URL http://link.springer.com/10.1007/978-3-319-61261-4.

[109] Deborah L. M. Rupert, Ganesh V. Shelke, Gustav Emilsson, Virginia Claudio, Stephan Block, Cecilia Lässer, Andreas Dahlin, Jan O. Lötvall, Marta Bally, Vladimir P. Zhdanov, and Fredrik Höök. Dual-Wavelength Surface Plasmon Resonance for Determining the Size and Concentration of Sub-Populations of Extracellular Vesicles. *Analytical Chemistry*, 88(20):9980–9988, October 2016. ISSN 0003-2700, 1520-6882. doi: 10.1021/acs.analchem.6b01860. URL https://pubs.acs.org/doi/10.1021/acs.analchem.6b01860.

[110] Igor N. Serdyuk, Nathan R. Zaccai, and Joseph Zaccai. Surace plasmon resonance and interferometry-based biosensors. In *Methods in Molecular Biophysics*, pages 234–250. Cambridge University P9ress, 2007. ISBN 978-0-521-81524-6.

[111] Erik Reimhult, Charlotte Larsson, Bengt Kasemo, and Fredrik Höök. Simultaneous Surface Plasmon Resonance and Quartz Crystal Microbalance with Dissipation Monitoring Measurements of Biomolecular Adsorption Events Involving Structural Transformations and Variations in Coupled Water. *Analytical Chemistry*, 76(24):7211–7220, December 2004. ISSN 0003-2700, 1520-6882. doi: 10.1021/ac0492970. URL https://pubs.acs.org/doi/10.1021/ac0492970.

[112] R. Barer and S. Joseph. Refractometry of living cells part I. basic principles. *Journal of Cell Science*, S3-95(32):399–423, December 1954. ISSN 0021-9533, 1477-9137. doi: 10.1242/jcs.s3-95.32.399. URL https://journals.biologists.com/jcs/article/s3-95/32/399/64106/Refractometry-of-living-cells-part-I-basic.

[113] Robert Pecora, editor. *Dynamic Light Scattering: Applications of Photon Correlation Spectroscopy*. Springer US, Boston, MA, 1985. ISBN 978-1-4612-9459-7 978-1-4613-2389-1. doi: 10.1007/978-1-4613-2389-1. URL http://link.springer.com/10.1007/978-1-4613-2389-1.

[114] Frank Babick. Dynamic light scattering (DLS). In *Characterization of Nanoparticles*, pages 137–172. Elsevier, 2020. ISBN 978-0-12-814182-3. doi: 10.1016/B978-0-12-814182-3.00010-9. URL https://linkinghub.elsevier.com/retrieve/pii/B9780128141823000109.

[115] Buddy D. Ratner, Allan S. Hoffman, Frederick j. Schoen, and Jack E. Lemons. Classes of Materials Used in Medicine. In *Biomaterials Science*, pages 37–131. Academic Press, 1996. ISBN 0-12-582460-0.

[116] Isabel U. Foreman-Ortiz, Ting Fung Ma, Brandon M. Hoover, Meng Wu, Catherine J. Murphy, Regina M. Murphy, and Joel A. Pedersen. Nanoparticle tracking analysis and statistical mixture distribution analysis to quantify

nanoparticle–vesicle binding. *Journal of Colloid and Interface Science*, 615: 50–58, June 2022. ISSN 00219797. doi: 10.1016/j.jcis.2022.01.141. URL https://linkinghub.elsevier.com/retrieve/pii/S002197972200159X.

[117] Su Gao, Shuangshuang Chen, and Qinghua Lu. Real-Time Profiling of Anti-(Epithelial Cell Adhesion Molecule)-Based Immune Capture from Molecules to Cells Using Multiparameter Surface Plasmon Resonance. *Langmuir*, 35(4):1040–1046, January 2019. ISSN 0743-7463, 1520-5827. doi: 10.1021/acs.langmuir.8b03898. URL https://pubs.acs.org/doi/10.1021/acs.langmuir.8b03898.

[118] Xucheng Hou, Tal Zaks, Robert Langer, and Yizhou Dong. Lipid nanoparticles for mRNA delivery. *Nature Reviews Materials*, 6(12):1078–1094, August 2021. ISSN 2058-8437. doi: 10.1038/s41578-021-00358-0. URL https://www.nature.com/articles/s41578-021-00358-0.

[119] Sean A. Dilliard and Daniel J. Siegwart. Passive, active and endogenous organ-targeted lipid and polymer nanoparticles for delivery of genetic drugs. *Nature Reviews Materials*, 8(4):282–300, January 2023. ISSN 2058-8437. doi: 10.1038/s41578-022-00529-7. URL https://www.nature.com/articles/s41578-022-00529-7.

[120] Joel G Rurik, István Tombácz, Amir Yadegari, Pedro O Méndez Fernández, Swapnil V Shewale, Li Li, Toru Kimura, Ousamah Younoss Soliman, Tyler E Papp, Ying K Tam, Barbara L Mui, Steven M Albelda, Ellen Puré, Carl H June, Haig Aghajanian, Drew Weissman, Hamideh Parhiz, and Jonathan A Epstein. CAR T cells produced in vivo to treat cardiac injury. *Science*, 375(6575):91–96, January 2022. doi: 10.1126/science.abm059. URL https://www.science.org/doi/10.1126/science.abm0594.

[121] Laura E. Swart, Marcel H. A. M. Fens, Anita Van Oort, Piotr Waranecki, L. Daniel Mata Casimiro, David Tuk, Martijn Hendriksen, Luca Van Den Brink, Elizabeth Schweighart, Cor Seinen, Ryan Nelson, Anja Krippner-Heidenreich, Tom O'Toole, Raymond M. Schiffelers, Sander Kooijmans, and Olaf Heidenreich. Increased Bone Marrow Uptake and Accumulation of Very-Late Antigen-4 Targeted Lipid Nanoparticles. *Pharmaceutics*, 15(6):1603, May 2023. ISSN 1999-4923. doi: 10.3390/pharmaceutics15061603. URL https://www.mdpi.com/1999-4923/15/6/1603.

[122] Alaaldin M. Alkilany, Lin Zhu, Horst Weller, Alf Mews, Wolfgang J. Parak, Matthias Barz, and Neus Feliu. Ligand density on nanoparticles: A parameter with critical impact on nanomedicine. *Advanced Drug Delivery Reviews*, 143: 22–36, March 2019. ISSN 0169409X. doi: 10.1016/j.addr.2019.05.010. URL https://linkinghub.elsevier.com/retrieve/pii/S0169409X19300602.

[123] Chaoxiang Chen, Yingxing Zhou, Chen Chen, Shaobin Zhu, and Xiaomei Yan. Quantification of Available Ligand Density on the Surface of Targeted Liposomal Nanomedicines at the Single-Particle Level. *ACS Nano*, 16(4):6886–6897, April 2022. ISSN 1936-0851, 1936-086X. doi: 10.1021/acsnano.2c02084. URL https://pubs.acs.org/doi/10.1021/acsnano.2c02084.

[124] Lisa Belfiore, Lisanne M. Spenkelink, Marie Ranson, Antoine M. Van Oijen, and Kara L. Vine. Quantification of ligand density and stoichiometry on the surface of liposomes using single-molecule fluorescence imaging. *Journal of Controlled Release*, 278:80–86, May 2018. ISSN 01683659. doi: 10.1016/j.jconrel.2018.03.022. URL https://linkinghub.elsevier.com/retrieve/pii/S0168365918301512.

[125] Vy Tran, Na Nguyen, Scott Renkes, Kytai T. Nguyen, Tam Nguyen, and George Alexandrakis. Current and Near-Future Technologies to Quantify Nanoparticle Therapeutic Loading Efficiency and Surface Coating Efficiency with Targeted Moieties. *Bioengineering*, 12(4):362, March 2025. ISSN 2306-5354. doi: 10.3390/bioengineering12040362. URL https://www.mdpi.com/2306-5354/12/4/362.

[126] CharlesE. Hoyle and ChristopherN. Bowman. Thiol–Ene Click Chemistry. *Angewandte Chemie International Edition*, 49(9):1540–1573, February 2010. ISSN 1433-7851, 1521-3773. doi: 10.1002/anie.200903924. URL https://onlinelibrary.wiley.com/doi/10.1002/anie.200903924.

[127] Hartmuth C. Kolb, M. G. Finn, and K. Barry Sharpless. Click Chemistry: Diverse Chemical Function from a Few Good Reactions. *Angewandte Chemie International Edition*, 40(11):2004–2021, June 2001. ISSN 1433-7851, 1521-3773. doi: 10.1002/1521-3773(20010601)40:11<2004::AID-ANIE2004>3.0.CO;2-5. URL https://onlinelibrary.wiley.com/doi/10.1002/1521-3773(20010601)40:11<2004::AID-ANIE2004>3.0.CO;2-5.

[128] Nobel Prize Outreach 2025. Nobel Prize in Chemistry 2022, . URL https://www.nobelprize.org/prizes/chemistry/2022/summary/.

[129] Jason E. Hein and Valery V. Fokin. Copper-catalyzed azide–alkyne cycloaddition (CuAAC) and beyond: new reactivity of copper(i) acetylides. *Chemical Society Reviews*, 39(4):1302, 2010. ISSN 0306-0012, 1460-4744. doi: 10.1039/b904091a. URL https://xlink.rsc.org/?DOI=b904091a.

[130] Hong Yeol Yoon, Donghyun Lee, Dong-Kwon Lim, Heebeom Koo, and Kwangmeyung Kim. Copper-Free Click Chemistry: Applications in Drug Delivery, Cell Tracking, and Tissue Engineering. *Advanced Materials*, 34(10):2107192, March 2022. ISSN 0935-9648, 1521-4095. doi: 10.1002/adma.202107192. URL https://onlinelibrary.wiley.com/doi/10.1002/adma.202107192.

[131] Maximilian W Popp, John M Antos, Gijsbert M Grotenbreg, Eric Spooner, and Hidde L Ploegh. Sortagging: a versatile method for protein labeling. *Nature Chemical Biology*, 3(11):707–708, November 2007. ISSN 1552-4450, 1552-4469. doi: 10.1038/nchembio.2007.31. URL https://www.nature.com/articles/nchembio.2007.31.